Density functional theories and molecular simulations of adsorption and phase transitions in nanopores

Peter I. Ravikovitch, Aleksey Vishnyakov, and Alexander V. Neimark*
Center for Modeling and Characterization of Nanoporous Materials, TRI/Princeton, 601 Prospect Avenue, Princeton, New Jersey 08542
(Received 29 December 2000; published 20 June 2001)

The nonlocal density functional theory (NLDFT) of confined fluids is tested against Monte Carlo simulations by using the example of Lennard-Jones (LJ) fluid sorption in slit-shaped and cylindrical nanopores ranging from 0.3 to 10 nm in width. The fluid-fluid and solid-fluid parameters of the LJ potentials were chosen to represent several experimentally important adsorption systems: nitrogen and carbon dioxide in activated carbons, zeolites, and mesoporous molecular sieves of the MCM-41 type. Freezing in nanopores is discussed using the example of methane sorption in carbon at 111 K. Comparison with reference experiments is given when available. Two versions of NLDFT, the smoothed density approximation and the fundamental measure theory, are considered. It is shown that NLDFT approaches with properly chosen parameters provide quantitative agreement with the results of Monte Carlo simulations and reference experiments. Appreciable deviations are found in extremely narrow pores of less than two molecular diameters in width. In wider pores, NLDFT models can be used for quantitative predictions of reversible and hysteretic adsorption isotherms and analyses of the specifics of phase transformations, including the equilibrium and spinodal phase transitions.

DOI: 10.1103/PhysRevE.64.011602 PACS number(s): 68.43.−h, 02.50.Ng, 64.70.Fx

I. INTRODUCTION

Nonlocal density functional theory (NLDFT) has proved to be a useful tool for studies of classical inhomogeneous fluids [1–7] (for a review, see [8]). It is well documented that NLDFT accurately describes the structure of simple confined fluids, i.e., the oscillating density profiles near solid surfaces [9–13,14], or of fluids in simple confining geometries, such as slits [15–18], cylinders [19–21], and spheres [12,22–24]. The nonlocal theory is a significant improvement as compared to the local DFT models [25,26]. NLDFT models are widely employed in the modern literature for theoretical predictions of adsorption isotherms in nanoporous materials and phase transitions in confining geometries, especially capillary condensation, layering, and wetting transitions of simple fluids in pores [10,18–20,27–51] (see review [50]). NLDFT based methods for pore size characterization were developed and implemented in commercial adsorption instruments [52–54]. In our previous papers, we have shown several striking examples of the quantitative agreement between the NLDFT, Monte Carlo (MC) simulations, and adsorption experiments on regular materials, provided that both the NLDFT and the simulation methods quantitatively describe the experimental bulk two-phase equilibrium, surface tension included, and the adsorption isotherm on a nonporous reference substrate [43,51,55–57]. Nevertheless, the limits of applicability of mean field NLDFT methods and their accuracy for quantitative description of experimental systems are still under discussion. The purpose of this paper is to give a systematic comparison between NLDFT calculations and MC simulations of the adsorption isotherms and phase transitions in various systems.

The extensive literature on testing different DFT approaches versus molecular simulations provides many examples of both agreement and disagreement in the description of the fluid structure and phase transitions in confined fluids. The main difficulty is that the approximations made in the DFT's inevitably lead to a difference in the bulk phase diagram as compared with the benchmark MC simulations [32,35,58,59]. These discrepancies complicate the comparison of DFT and simulations, and may significantly affect the predicted adsorption isotherms and coexistence phase diagrams.

Many authors have compared the DFT and simulated adsorption isotherms at the same absolute reduced temperatures and absolute densities. For example, Kozak and Sokolowski [34] used the functional of Kierlik and Rosinberg [7] and grand canonical MC (GCMC) simulations to study wetting and capillary condensation transitions in slit pores. They obtained good agreement for the density profiles; however, only qualitative agreement was found for the adsorption isotherms and the capillary condensation transitions. Other authors [37,47] compared the capillary condensation isotherms in DFT and simulations using reduced pressure, related to the pressure P_0 of vapor-liquid coexistence in the bulk fluid. Lastoskie *et al.* [37,47] studied the adsorption of Lennard-Jones (LJ) nitrogen in slit pores of carbon with NLDFT and the Gibbs ensemble MC method [60,61], and found quantitative agreement for the adsorption isotherms and vapor-liquid equilibrium in these systems. Peterson *et al.* [20] applied the NLDFT of Tarazona [1,4] to study adsorption of a LJ fluid in cylindrical pores with nonwetting walls. They compared the NLDFT and GCMC isotherms at the same reduced temperature T/T_c^{bulk}, i.e., the temperature related to the bulk critical temperature T_c^{bulk}, and the same relative pressure P/P_0. The capillary condensation transitions and qualitatively similar phase diagrams were determined for a series of pores ranging from 1 to 10 diameters of the fluid

*Author to whom correspondence should be addressed. Electronic address: aneimark@triprinceton.org

molecule. For a number of pores considered by Peterson *et al.* [20], the density of the condensed liquidlike phase, as well as the conditions of vapor-liquid equilibria and spontaneous capillary condensation and desorption, obtained using the NLDFT, deviated significantly from the results of the corresponding GCMC simulations. Kierlik *et al.* calculated the adsorption equilibrium for binary LJ mixtures in slit-shaped pores [35] and obtained very good agreement with the benchmark GCMC simulation for the adsorption isotherms and selectivity at pressures well below the pressure of vapor-liquid equilibrium in the bulk. Essentially quantitative agreement at higher pressures was obtained by comparing the NLDFT and GCMC results at the same relative pressures and by scaling the adsorption isotherm by the monolayer density [35]. Many attempts have been made to correct the deficiencies of the mean field DFT either by considering improved free energy functionals for both inhomogeneous and homogeneous situations [62,63], or by introducing corrections to the bulk equation of state to fit the simulation data [32,38,41,59,64].

In this paper we adopt a different approach: the approximations made in the DFT description of the free energy are corrected by adjusting the parameters of the intermolecular fluid-fluid potential. In particular, we require both (DFT and MC) molecular models to give the best fit to the bulk thermodynamic properties of the experimental fluid of interest. These include the liquid and vapor densities, saturation pressures, and interfacial tension. Such parametrization allows one simultaneously to make consistent comparisons between the theory and simulations for systems important in practice, and to compare the theoretical and simulated results with the available reference experimental data. Our procedure leads to slightly different sets of fluid-fluid interaction parameters employed in the NLDFT compared to those in the MC simulations. The solid-fluid parameters are the same in theory and simulations, and are determined from the fit to the reference adsorption isotherms on nonporous substrates.

The paper is structured as follows. In Sec. II, we describe the theory, the molecular models used, and the proposed procedure for consistent selection of the fluid-fluid and solid-fluid interaction parameters. Two versions of NLDFT with different density functionals for hard spheres are considered: the smoothed density approximation (SDA) of Tarazona [1,4] and the fundamental measure theory (FMT) of Rosenfeld-Kierlik-Rosinberg [6,7]. A recently developed canonical ensemble version of NLDFT (CEDFT) [46] is employed to trace the unstable sections of the sigmoid-shaped capillary condensation isotherms between the vaporlike and liquidlike spinodals. This technique is compared with the canonical ensemble MC (CEMC) simulation complemented by the Widom particle insertion method [65].

In Sec. III we present the NLDFT and MC results, in comparison with experimental data where available. The structure of hard-sphere fluids is discussed in Sec. III A. In Secs. III B and III C, we describe the vapor-liquid phase diagrams for bulk LJ fluids and the liquid-vapor surface tension predicted by MC and DFT models. Nitrogen adsorption isotherms at 77 K on open surfaces of carbon and silica are presented in Sec. III D. Nitrogen capillary condensation at 77 K in the slit-shaped pores of carbonaceous adsorbents and the cylindrical pores of MCM-41 materials is discussed in Sec. III E. We also consider two examples of ''extreme confinement'' with the goal of testing the behavior of different versions of NLDFT: freezing of methane at 111 K in carbon slit pores (Sec. III G) and carbon dioxide adsorption at 273 K in cylindrical micropores of zeolites (Sec. III F). The results are summarized in Sec. IV. We found that, in general, NLDFT predicts the reversible and hysteretic adsorption isotherms and the full phase diagrams of capillary condensation including the points of phase equilibrium and spinodal transitions in good agreement with the MC simulations and reference experiments. Appreciable deviations between the theory and simulations were found only in extremely narrow pores of less than two molecular diameters in width.

II. THEORETICAL METHODS

A. Nonlocal density functional theory

1. General approach

Density functional theory implies that the Helmholtz free energy of an inhomogeneous fluid $F[\rho(\mathbf{r})]$ is expressed as a functional of the local density $\rho(\mathbf{r})$ [44,66]:

$$F[\rho(\mathbf{r})]=F_{\mathrm{int}}[\rho(\mathbf{r})]+\int d\mathbf{r}\,\rho(\mathbf{r})U_{\mathrm{ext}}(\mathbf{r}). \tag{1}$$

Here $F_{\mathrm{int}}[\rho(\mathbf{r})]$ is the intrinsic Helmholtz free energy and $U_{\mathrm{ext}}(\mathbf{r})$ is the external potential imposed by the pore walls. The intrinsic free energy is composed of the ideal gas free energy, which is given by an exact expression, and the excess free energy $F_{\mathrm{ex}}[\rho(\mathbf{r})]$, which accounts for the interparticle interactions:

$$F_{\mathrm{int}}[\rho(\mathbf{r})]=\beta^{-1}\int d\mathbf{r}\,\rho(\mathbf{r})\{\ln[\Lambda^3\rho(\mathbf{r})]-1\}+F_{\mathrm{ex}}[\rho(\mathbf{r})]. \tag{2}$$

Here $\beta^{-1}=k_BT$ is the temperature and $\Lambda=\sqrt{2\pi mk_BT/h^2}$ is the thermal de Broglie wavelength. Successive functional differentiation of the excess free energy generates a hierarchy of direct correlation functions. In particular, the one-particle direct correlation function is given by

$$c^{(1)}(\mathbf{r};[\rho])=-\beta\frac{\delta F_{\mathrm{ex}}[\rho]}{\delta\rho(\mathbf{r})}; \tag{3a}$$

the two-particle direct correlation function is given by

$$c^{(2)}(\mathbf{r},\mathbf{r}';[\rho])=-\beta\frac{\delta^2F_{\mathrm{ex}}[\rho]}{\delta\rho(\mathbf{r})\rho(\mathbf{r}')}. \tag{3b}$$

In the conventional DFT the system is considered in the grand canonical ensemble, at constant volume (geometry), temperature, and chemical potential μ. The density distribution is obtained by minimization of the grand thermodynamic potential Ω,

$$\Omega[\rho(\mathbf{r})]=F[\rho(\mathbf{r})]-\int d\mathbf{r}\,\rho(\mathbf{r})\mu, \tag{4}$$

which leads to the Euler-Lagrange equation for the density profile:

$$\rho(\mathbf{r})=\Lambda^{-3}\exp\{c^{(1)}(\mathbf{r};[\rho])+\beta\mu-\beta U_{\mathrm{ext}}(\mathbf{r})\}. \tag{5}$$

Recently, we proposed the canonical ensemble density functional theory, which implies minimization of the Helmholtz free energy $F[\rho(\mathbf{r})]$ at given mean fluid density,

$$\langle\rho\rangle=\int d\mathbf{r}\,\rho(\mathbf{r}), \tag{6}$$

i.e., in the *NVT* ensemble. Here, the chemical potential of the desired equilibrium state is initially unknown and determined in the process of simultaneous solution of Eqs. (5) and (6) [46]. While applying CEDFT, we do not consider systems with a small number of molecules, for which the results of the grand canonical and canonical ensembles may differ [24].

The excess free energy of an inhomogeneous system, $F_{\mathrm{ex}}[\rho(\mathbf{r})]$, is a unique but unknown functional of the local particle density. Various DFT versions give approximate expressions for $F_{\mathrm{ex}}[\rho(\mathbf{r})]$. For fluids with attractive interactions such as the LJ fluid, the excess free energy is decomposed into the contribution from a reference system of hard spheres, and the free energy due to attractive interactions,

$$F_{\mathrm{ex}}[\rho(\mathbf{r})]=F_{\mathrm{HS}}[\rho(\mathbf{r})]+F_{\mathrm{attr}}[\rho(\mathbf{r})]. \tag{7}$$

The attractive interactions are usually considered as in the first-order Weeks-Chandler-Andersen (WCA) [67] perturbation theory of bulk fluids, or the first- or second-order Barker-Henderson (BH) theory [68,69]. In these approaches, the intermolecular potential is divided into the repulsive and attractive contributions. The repulsive interactions are then approximated by a hard-sphere functional with a certain choice of the hard-sphere diameter. Given that the pair-correlation function of the inhomogeneous fluid is unknown, the attractive interactions are treated in most cases in a mean field fashion.

The free energy functionals for hard spheres play a central role in DFT. Several functionals for inhomogeneous hard-sphere fluids have been developed. In perturbative DFT's, the direct correlation function of an inhomogeneous system is expanded about a slowly varying reference density [3,13,70,71]. The expansion is usually truncated after the second [3,70,71] or third [9] order. Recent approaches employ the universality properties of the bridge functional [14,72]. In nonperturbative DFT's, such as the weighted density approximation [2,5], the smoothed density approximation [1,4], and fundamental measure theory [6,7] the excess free energy is calculated using coarse-grained or smoothed density(ies). The weighting functions are either found from the fit of the pair-correlation function in the homogeneous fluid limit [1], or consistently predicted by the theory itself [6,7,73].

Below we consider two versions of NLDFT that are currently employed in practical calculations of adsorption isotherms and pore size distributions in nanoporous materials: the smoothed density approximation of Tarazona [1,4], and the fundamental measure theory of Rosenfeld-Kierlik-Rosinberg [6,7,74] and modifications of the latter [73].

2. The smoothed density approximation

In this approximation [1,4] the free energy of the hard-sphere fluid is evaluated at the smoothed density $\overline{\rho}(\mathbf{r})$:

$$F_{\mathrm{HS}}[\rho(\mathbf{r})]=\int d\mathbf{r}\,\rho(\mathbf{r})f_{\mathrm{HS}}[\overline{\rho}(\mathbf{r});d_{\mathrm{HS}}]. \tag{8}$$

Here $f_{\mathrm{HS}}[\overline{\rho}(\mathbf{r});d_{\mathrm{HS}}]$ is the excess free energy per particle, which is calculated from the Carnahan-Starling (CS) equation of state [75]. The smoothed density is defined as

$$\overline{\rho}(\mathbf{r})=\int d\mathbf{r}'\,\rho(\mathbf{r}')w(|\mathbf{r}-\mathbf{r}'|,\overline{\rho}(\mathbf{r})), \tag{9}$$

where $w(|\mathbf{r}-\mathbf{r}'|,\overline{\rho}(\mathbf{r}))$ is the weighting function. Tarazona proposed the following expansion for the weighting function:

$$w(r,\rho)=w_0(r)+w_1(r)\rho+w_2(r)\rho^2. \tag{10}$$

The coefficients $w_0(r)$, $w_1(r)$, and $w_2(r)$ were found from the requirement that the functional approximates the Percus-Yevick (PY) two-particle direct correlation function of the homogeneous hard-sphere fluid [69]. Explicit expressions for the weighting functions are given in Ref. [4].

The resulting expression for the direct correlation function $c^{(1)}(\mathbf{r};[\rho])$ to be used in Eq. (5) takes the form [76]

$$c^{(1)}(\mathbf{r};[\rho])=-\beta f_{\mathrm{HS}}[\overline{\rho}(\mathbf{r})]+\beta\int d\mathbf{r}'\lambda(\mathbf{r}')w(|\mathbf{r}-\mathbf{r}'|,\overline{\rho}(\mathbf{r}')), \tag{11}$$

where

$$\lambda(\mathbf{r})=-\rho(\mathbf{r})\frac{df_{\mathrm{HS}}[\overline{\rho}(\mathbf{r})]}{d\overline{\rho}}\Bigg/\left\{1-\int d\mathbf{r}'\,\rho(\mathbf{r}')\frac{dw(|\mathbf{r}-\mathbf{r}'|,\overline{\rho}(r))}{d\overline{\rho}(\mathbf{r})}\right\}. \tag{12}$$

3. Fundamental measure theory

In the FMT approach [6], the structure and thermodynamics of the hard-sphere fluid are predicted by the theory itself, based on fundamental geometrical measures of particles. FMT reduces to the Percus-Yevick [77] theory in the homogeneous fluid limit. Kierlik and Rosinberg (KR) [7] developed an equivalent [74] version of the FMT functional, which utilizes different forms of weighting functions.

Among the advantages of the FMT approach are that (1) it is almost free from *ad hoc* assumptions; (2) its extension to mixtures is straightforward, unlike that in Tarazona's theory [29]; (3) improved FMT formulations give correct dimensional crossover, i.e., they comply with the exact results for reduced dimensionality systems such as a two-dimensional (2D) hard-disk fluid, a 1D hard-rod fluid, and an effectively 0D fluid in a spherical cavity [73,78]. These properties are important for the description of crystallization and extreme confinements.

In the FMT, the excess free energy of the hard-sphere fluid has the form

$$F_{\mathrm{HS}}[\rho(\mathbf{r})]=\beta^{-1}\int d\mathbf{r}'\,\Phi[n_\alpha(\mathbf{r})]. \tag{13}$$

Here $\Phi[n_\alpha(\mathbf{r})]$ is the excess free energy density, which depends on the weighted densities $n_\alpha(\mathbf{r})$:

$$n_\alpha(\mathbf{r})=\int d\mathbf{r}'\,\rho(\mathbf{r}')\omega^{(\alpha)}(\mathbf{r}-\mathbf{r}'). \tag{14}$$

The weighting functions $\omega^{(\alpha)}(r)$ depend on the fundamental geometrical measures of the particles, such as volume, area, etc. The original Rosenfeld formulation [6] utilizes four scalar weighting functions

$$\omega^{(3)}(r)=\Theta(R-r),\quad \omega^{(2)}(r)=\left|\nabla\omega^{(3)}(r)\right|=\delta(R-r), \tag{15a}$$

$$\omega^{(1)}(r)=\frac{\omega^{(2)}(r)}{4\pi R},\quad \omega^{(0)}(r)=\frac{\omega^{(2)}(r)}{4\pi R^2} \tag{15b}$$

and two vector weighting functions

$$\omega^{(V2)}(\mathbf{r})=-\nabla\omega^{(3)}(r)=\frac{\mathbf{r}}{r}\,\delta(R-r), \tag{15c}$$

$$\omega^{(V1)}(r)=\frac{\omega^{(V2)}(r)}{4\pi R}. \tag{15d}$$

In the above, $\Theta(r)$ is the Heaviside step function, and $\delta(r)$ is the Dirac delta function.

In the uniform fluid $\rho(\mathbf{r})\equiv\rho$ and the weighted densities coincide with the variables of the scaled particle theory [69]:

$$n_0=\rho,\quad n_1=R\rho,\quad n_2=4\pi R^2\rho,\quad n_3=4/3\pi R^3\rho, \tag{16}$$

where R is the hard-sphere radius.

The one-particle direct correlation function of a nonuniform fluid to be used in Eq. (5) is given by

$$c^{(1)}(r)=-\beta\frac{\delta F_{\mathrm{HS}}[\rho]}{\delta\rho(r)}=-\int dr'\sum_\alpha\frac{\partial\Phi}{\partial n_\alpha}\omega^{(\alpha)}(r-r'). \tag{17}$$

The free energy density is given by the expression

$$\Phi=-n_0\ln(1-n_3)+\frac{n_1n_2-\mathbf{n}_{V1}\cdot\mathbf{n}_{V2}}{1-n_3}+\frac{\frac{1}{3}n_2^3-n_2(\mathbf{n}_{V2}\cdot\mathbf{n}_{V2})}{8\pi(1-n_3)^2}. \tag{18}$$

Here $\mathbf{n}_{V1}$ and $\mathbf{n}_{V2}$ are vectors. In the limit of a homogeneous fluid the PY expression for the free energy [77] is recovered. The first term in Eq. (18) is the exact free energy of the one-dimensional hard-rod fluid [79]. The first two terms of Eq. (18) give a quite accurate representation of the free energy of the hard-disk fluid. Corrections to the third term have been proposed to improve the behavior of the functional in situations of reduced dimensionality [73]. Two versions of the corrected third term of Eq. (18) are considered. The first modification has the form

$$\Phi_3=\frac{\frac{1}{3}n_2^3}{8\pi(1-n_3)^2}(1-\xi^2)^q \tag{19}$$

with $q=2$ or 3. In analogy with the authors of [80] we refer to this modified form as RSLT1 ($q=2,3$). The second modification is called RSLT2:

$$\Phi_3=\frac{\frac{1}{3}n_2^3}{8\pi(1-n_3)^2}(1-3\xi^2+2\xi^3). \tag{20}$$

All these corrections have only marginal effects in three-dimensional situations. In this work we do not consider the most recent modifications to the FMT functional, which require tensorial quantities in the weighting functions [78].

4. Attractive interactions and bulk phase diagrams

In the mean field approximation the attractive interactions are

$$F_{\mathrm{attr}}[\rho(\mathbf{r})]=\frac{1}{2}\int\int d\mathbf{r}\,d\mathbf{r}'\rho(\mathbf{r})\rho(\mathbf{r}')\Phi_{\mathrm{attr}}(|\mathbf{r}-\mathbf{r}'|). \tag{21}$$

Here $\Phi_{\mathrm{attr}}(r)$ is the attractive part of the LJ potential. The bulk fluid is described by the following equations of state:

$$\mu(\rho)=\mu_{\mathrm{HS}}(\rho)+\rho\int d\mathbf{r}\,\Phi_{\mathrm{attr}}(\mathbf{r}), \tag{22}$$

$$P(\rho)=P_{\mathrm{HS}}(\rho)+\frac{1}{2}\rho^2\int d\mathbf{r}\,\Phi_{\mathrm{attr}}(\mathbf{r}), \tag{23}$$

where $\mu_{\mathrm{HS}}(\rho)$ and $P_{\mathrm{HS}}(\rho)$ are the chemical potential and the pressure of the hard-sphere fluid, respectively. The equilibrium conditions are determined from the equality of pressures and chemical potentials in the two phases. Simultaneous solution of Eqs. (22) and (23) gives the equilibrium gas density, the equilibrium liquid density, the chemical potential at coexistence, and the saturation vapor pressure.

In the SDA, $\mu_{\mathrm{HS}}(\rho)$ and $P_{\mathrm{HS}}(\rho)$ are calculated from the CS equation [75], while in the FMT theory they are calcu-

lated from the PY equation [77]. The difference between the results of the CS and PY equations at high densities, however, leads to only minor differences in the predicted two-phase bulk diagrams.

The integrated strength of attractive interactions of the truncated LJ fluid is

$$\int_{|\mathbf{r}|<r_c} d\mathbf{r}\,\Phi_{\mathrm{attr}}(\mathbf{r}) = -\alpha\frac{32}{9}\pi\epsilon_{ff}\sigma_{ff}^3 + \frac{16}{3}\pi\epsilon_{ff}\sigma_{ff}^3\left[\left(\frac{\sigma_{ff}}{r_c}\right)^3 - \frac{1}{3}\left(\frac{\sigma_{ff}}{r_c}\right)^9\right], \tag{24}$$

where r_c is a cutoff distance; $\alpha=1$ when the LJ potential is split according to the BH decomposition [68] and $\sqrt{2}$ when the potential is split according to the WCA scheme [67],

$$\Phi_{\mathrm{attr}}(r) = \begin{cases} -\epsilon_{ff}, & r<r_m=2^{1/6}\sigma_{ff} \\ 4\epsilon_{ff}[(\sigma_{ff}/r)^{12}-(\sigma_{ff}/r)^6], & r_m<r<r_c \\ 0, & r>r_c. \end{cases} \tag{25}$$

The first term of Eq. (24) is the strength of attractive interactions of the full LJ fluid, and the second term is the correction due to the potential cutoff, which is quite small but not negligible even for $r_c=5$.

Two prescriptions for the choice of the hard-sphere diameter are usually considered. The first one is the well-known BH expression [68]. The second one originates from the works of Verlet and Weis [81] and Lu, Evans, and Da Gama [82]:

$$d_{\mathrm{HS}} = \sigma_{ff}\frac{\eta_1 k_B T/\epsilon_{ff} + \eta_2}{\eta_3 k_B T/\epsilon_{ff} + \eta_4}. \tag{26}$$

The coefficients $\eta_1=0.3837$, $\eta_2=1.035$, $\eta_3=0.4249$, and $\eta_4=1$ reported in Ref. [26] fit the liquid branch of the phase diagram of the simulated LJ fluid.

The equation of state given by Eqs. (22) and (23) is essentially a two-parameter equation that depends on the diameter of the hard spheres d_{HS} and the product $(\epsilon_{ff}\sigma_{ff}^3)$. This mean field approximation gives a poor description of the bulk phase diagram of the LJ fluid, especially near the critical temperature. The BH separation [68] leads to a bulk phase diagram with a lower critical temperature than the LJ fluid critical temperature [62]. In contrast, the WCA separation overestimates the critical temperature (see Sec. III).

Many attempts have been made to improve the agreement between the theory and simulations for the bulk phase diagram. For studies of wetting and drying transitions at wall-fluid interfaces, van Swol and Henderson have fitted the bulk equation of state to the simulation data by adding a polynomial term to the free energy of the hard spheres [32]. Bruno, Caccamo, and Tarazona [64] and then Velasco and Tarazona [59] proposed adjustments to the mean field attractive term to get a better agreement with the simulations for the bulk phase diagrams. Effective attractive interactions as proposed by Velasco and Tarazona [59] have the form

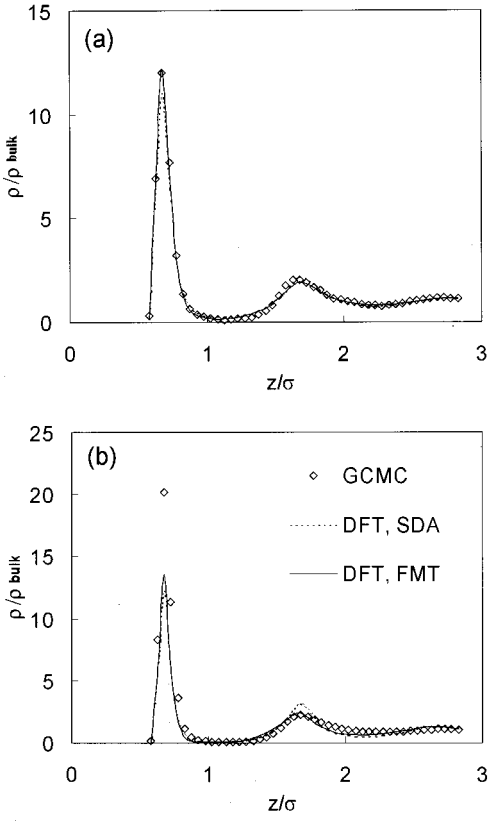

FIG. 1. Density profiles of hard-sphere fluid near 9-3 attractive wall. Points, simulations of Sokolowski and Fischer [9]; solid line, NLDFT calculations using SDA functional; dotted line, NLDFT using FMT functional. (a) $\rho_{\mathrm{bulk}}=0.4658$, $\epsilon_{sf}/kT=0.2876$, $T=150\,\mathrm{K}$; (b) $\rho_{\mathrm{bulk}}=0.6059$, $\epsilon_{sf}/kT=0.1917$, $T=100\,\mathrm{K}$. In both cases $\sigma_{sf}/\sigma_{ff}=0.5621$.

$$\Phi_{\mathrm{attr}}(r) = \begin{cases} -\epsilon_{ff}/\lambda, & r<(2\lambda)^{1/6}\sigma_{ff} \\ 4\epsilon_{ff}[\lambda(\sigma_{ff}/r)^{12}-(\sigma_{ff}/r)^6], & (2\lambda)^{1/6}\sigma_{ff}<r<r_c \\ 0, & r>r_c, \end{cases} \tag{27}$$

which leads to

$$\int_{|\mathbf{r}|<r_c} d\mathbf{r}\,\Phi_{\mathrm{attr}}(\mathbf{r}) = -\frac{32}{9}\pi\sqrt{2/\lambda}\epsilon_{ff}\sigma_{ff}^3 + \frac{16}{3}\pi\epsilon_{ff}\sigma_{ff}^3\left[\left(\frac{\sigma_{ff}}{r_c}\right)^3 - \frac{\lambda}{3}\left(\frac{\sigma_{ff}}{r_c}\right)^9\right]. \tag{28}$$

This approach was adopted by Kierlik *et al.* in their studies of liquid mixtures in pores [38,41]. In our experience, however, this prescription leads to an appreciable overestimation of attractive interactions, which in turn leads to predictions

for the capillary condensation transitions in pores with attractive walls occurring at significantly lower pressures than in the simulations.

More systematic ways to improve the description of attractive interactions include a version of DFT developed in the spirit of second-order BH perturbation theory [62], which gives a decent prediction of the bulk diagram, and good results for the density profiles [12,62]. Another way to treat attractive interactions was proposed by Mederos *et al.* [63], who used a local compressibility equation. The approach gave good results for the whole bulk phase diagram of the LJ fluid, solid phase included, although, the accuracy of this approach for confined fluids has not been tested.

In our work, we explicitly use the approximation (21) with the fluid-fluid interaction parameters chosen to provide the best fit with the experimental bulk phase diagram. As shown below, this approach leads to an accurate description of the real systems considered.

B. Monte Carlo simulations

Most of the MC simulations we have done in the grand canonical ensemble using the well-developed method of GCMC [83]. GCMC simulations are performed at a given chemical potential of the adsorbate μ. To present the adsorption isotherm in the standard variables of amount adsorbed versus vapor pressure, the latter is related to the chemical potential via the bulk equation of state. A suitable equation of state for the LJ fluid was derived by Johnson, Zollweg, and Gubbins [84].

We generated GCMC adsorption and desorption isotherms consequently by increasing or reducing the chemical potential. The final configuration obtained served as the initial state for the next simulation. The size of the simulation box in the directions parallel to pore walls was varied in order to estimate finite size effects. In these directions, periodic boundary conditions were applied. If not specified, the size of the basic MC cell was set to $10\sigma_{ff}$: The LJ potential was cut at $5\sigma_{ff}$. The lengths of Markov chains were approximately 5×10^4 configurations per molecule. Statistics on equilibrium properties of the system were collected over the last 2.5×10^4 configurations.

If the temperature is well below the capillary critical temperature, GCMC simulations produce a hysteresis loop bounded by vertical steps corresponding to spontaneous capillary condensation and desorption. The point of vapor-liquid coexistence in a pore is located somewhere between the points of the spontaneous transitions. The GCMC method does not allow one to calculate directly the phase equilibria conditions in pores. To determine the bulk pressure corresponding to vapor-liquid coexistence in the pores, we applied the thermodynamic integration method of Peterson and Gubbins [85]. The Peterson-Gubbins method implies the construction of a reversible trajectory of equilibrium states, composed of four parts: (1) the adsorption isotherm of vaporlike states in the pore, (2) a reversible adsorption at supercritical temperature, (3) a path of constant chemical potential corresponding to a thermodynamically stable liquid at the subcritical temperature of interest, and (4) the desorption isotherm of liquidlike states in the pore. The grand potential Ω is calculated separately for the capillary vapor and liquidlike phases via integration of the Gibbs adsorption equation along the selected trajectory. At equilibrium the grand potentials for the two phases coincide. In the present work $T=140\,\mathrm{K}$ $(kT/\epsilon=0.762)$ was chosen as the supercritical temperature for the Peterson-Gubbins integration.

To check the results of the canonical ensemble density functional theory we have implemented the canonical ensemble MC method. Simulations are performed in the *NVT* ensemble at a given number of molecules in the cell. The chemical potential is determined by the Widom insertion method [65]. With the CEMC method one can construct the full phase diagram, which includes stable, metastable, and unstable branches [86]. It is worth noting that we have recently developed a method for MC simulation studies of phase transitions in confined fluids named the gauge cell method [87]. The gauge cell method, described elsewhere [87], allows one to construct a continuous phase diagram equivalent to that produced by the CEMC method without using the Widom method for determination of the chemical potential.

C. Molecular models

We have performed NLDFT calculations and MC simulations of LJ fluids adsorbed in meso- and micropores. Adsorption in mesopores was studied on standard examples of nitrogen at the boiling temperature 77.4 K in carbon slit-shaped pores and straight cylindrical silica pores, representing the channels of MCM-41 materials. The carbon pores were modeled as infinite slits with parallel graphite walls. Nitrogen-carbon interactions were described by the 10-4-3 potential of Steele [88], which is widely used for modeling interactions of simple molecules with graphite:

$$U_{\mathrm{sf}}(z)=2\pi\rho_V\epsilon_{\mathrm{sf}}\sigma_{\mathrm{sf}}^2\Delta\left[\left(\frac{\sigma_{\mathrm{sf}}}{z}\right)^{10}-\left(\frac{\sigma_{\mathrm{sf}}}{z}\right)^{4}-\frac{\sigma_{\mathrm{sf}}^4}{3\Delta(0.61\Delta+z)^3}\right]. \tag{29}$$

Here $\rho_V=0.114\,\text{Å}^{-3}$ is the number density of carbon atoms in graphite, $\Delta=3.35\,\text{Å}$ is the interlayer spacing in graphite, and ϵ_{sf} and σ_{sf} are the energetic and scale parameters of the solid-fluid LJ potential. The potential field in pores includes contributions of two opposite walls, given by

$$U_{\mathrm{sf}}^{(\mathrm{total})}=U_{\mathrm{sf}}(z)+U_{\mathrm{sf}}(H_{\mathrm{CC}}-z), \tag{30}$$

where H_{CC} is the distance between the nuclei of the outer carbon atoms on opposite walls.

The solid-fluid potential in cylindrical pores was modeled as LJ interactions of the adsorbate molecule with a single structureless cylindrical layer of oxygen atoms in the pore wall [89]:

$$U_{sf}(r,R_{CC})=\pi^2\rho_s\epsilon_{sf}\sigma_{sf}^2\left\{\frac{63}{32}\left[\frac{R_{CC}-r}{\sigma_{sf}}\left(1+\frac{r}{R_{CC}}\right)\right]^{-10}\times F\left[-\frac{9}{2},-\frac{9}{2};1;\left(\frac{r}{R_{CC}}\right)^2\right]-3\left[\frac{R_{CC}-r}{\sigma_{sf}}\left(1+\frac{r}{R_{CC}}\right)\right]^{-4}\times F\left[-\frac{3}{2},-\frac{3}{2};1;\left(\frac{r}{R_{CC}}\right)^2\right]\right\}. \quad (31)$$

Here, r is the radial coordinate of the adsorbate molecule reckoned from the pore center, $R_{CC}=D_{CC}/2$ is the radial coordinate of the adsorption centers, ρ_s is the surface number density of the adsorption centers, and $F[\alpha,\beta;\gamma;\delta]$ is the hypergeometric series. As the pore width increases, this potential reduces to the 10-4 form of the potential with a plane of LJ centers.

The narrowest cylindrical micropores with strongly attractive walls are filled by N_2 at 77.4 K at a very low pressure that depends crucially on the pore width (a change in the pore width by 1 Å may correspond to a change in the pore filling pressure by several orders of magnitude). To study the peculiarities of the NLDFT modeling of the sorption in cylindrical micropores of zeolites, we considered the LJ parameters and conditions corresponding to CO_2 on silica at 273.2 K. CO_2 at 273.2 K is considered as a suitable molecular probe for ultramicroporous sorbents. Although CO_2 is known for a strong electrostatic contribution to the fluid structure and thermodynamic properties, the LJ model was found capable of representing the experimental data on the vapor-liquid equilibrium with acceptable accuracy. We found earlier that the CO_2 adsorption isotherms in carbon micropores at 273 K were in good agreement with those obtained from GCMC simulations using a realistic three-center model [54,57].

The excess adsorption in slit pores is calculated from the equilibrium density profile in the direction perpendicular to the pore walls $\rho(z)$:

$$N_S(\mu)=\frac{1}{2}\left(\int_0^{H_{CC}}\rho(z)dz-\rho_{bulk}(\mu)H_{ref}\right), \quad (32)$$

where μ is the chemical potential (or, equivalently, the relative pressure P/P_0), $\rho_{bulk}(\mu)$ is the bulk fluid density, and H_{ref} is a reference pore width. The need to use the excess adsorption arises from the fact that this quantity is measured experimentally [45]. The reference pore width, which is the position of the Gibbs dividing surface, should be chosen in the same way as in the experimental measurements, in most cases by using helium calibration [45].

In cylindrical geometry the excess adsorption is calculated from the radially symmetric density profile $\rho(r)$:

$$N_S(\mu)=\frac{2}{D_{CC}-\sigma_{ss}}\int_0^{D_{CC}/2}\rho(r)r\,dr-\frac{D_{ref}^2}{4(D_{CC}-\sigma_{ss})}\rho_{bulk}(\mu), \quad (33)$$

where D_{ref} is a reference pore diameter. Here adsorption is expressed per ''internal'' area of the pore, which is probed in the experimental measurements, using $\sigma_{ss}=2.76$ Å as an effective diameter for oxygen in silica. It should be noted that for all systems considered in this work $\rho_{bulk}(\mu)$ is a small quantity, and for not very large pore sizes the difference between the absolute and excess adsorption can be neglected.

III. RESULTS AND DISCUSSION

A. Hard spheres near an attractive wall

As a test system, we reproduce here the original NLDFT calculations of Kierlik and Rosinberg [7] in comparison with the benchmark GCMC results of Sokolowski and Fischer [9] for the density profiles of a hard-sphere fluid near the 9-3 attractive wall $U_{sf}(z)=3\sqrt{3}/2\epsilon_{sf}[(\sigma_{sf}/z)^9-(\sigma_{sf}/z)^3]$. Because the hard-sphere fluid is athermal, its structure near the wall is entirely determined by the density of the hard spheres in the equilibrium bulk phase and the ratios of the parameters of the solid-fluid potential to the hard-sphere diameter and temperature, σ_{sf}/σ_{ff} and ϵ_{sf}/kT. Two different systems were considered: (1) $\rho_{bulk}=0.4658$, $\epsilon_{sf}/kT=0.2876$ and (2) $\rho_{bulk}=0.6059$, $\epsilon_{sf}/kT=0.1917$; the ratio $\sigma_{sf}/\sigma_{ff}=0.5621$ was used for both systems.

The density profiles for the hard-sphere fluid are presented in Fig. 1. At the higher temperature and lower bulk density, both SDA and FMT density functionals represent the GCMC density profile very well [Fig. 1(a)]. However, in the denser system ($\rho_{bulk}=0.6059$) at lower reduced temperature the theoretical results show disagreement with the benchmark GCMC profile [9]. In particular, both SDA and FMT theories underestimate the ordering in the layer next to the wall [Fig. 1(b)]. Our calculations with the FMT functional are identical to the earlier calculations of Kierlik and Rosinberg (see Figs. 3 and 4 in Ref. [7]). Note also that the density profiles obtained by the SDA and FMT functionals for hard spheres are almost identical for both temperatures.

B. Phase equilibrium of bulk fluid

The choice of fluid-fluid and solid-fluid parameters is the most essential for the predictive capability of molecular models. The majority of authors who have discussed the consistency of DFT modeling and molecular simulations used the same sets of parameters in the DFT and MC calculations. Although this approach seems to be the most natural and straightforward, it may lead to substantial discrepancies even for the simplest systems, due to discrepancies in the bulk saturation pressures and other properties, such as densities of coexisting bulk phases or vapor-liquid surface tension, predicted differently by different models [20,35]. Indeed, the MC and DFT approaches yield different equations of state for the bulk fluid. This is demonstrated in Fig. 2, which

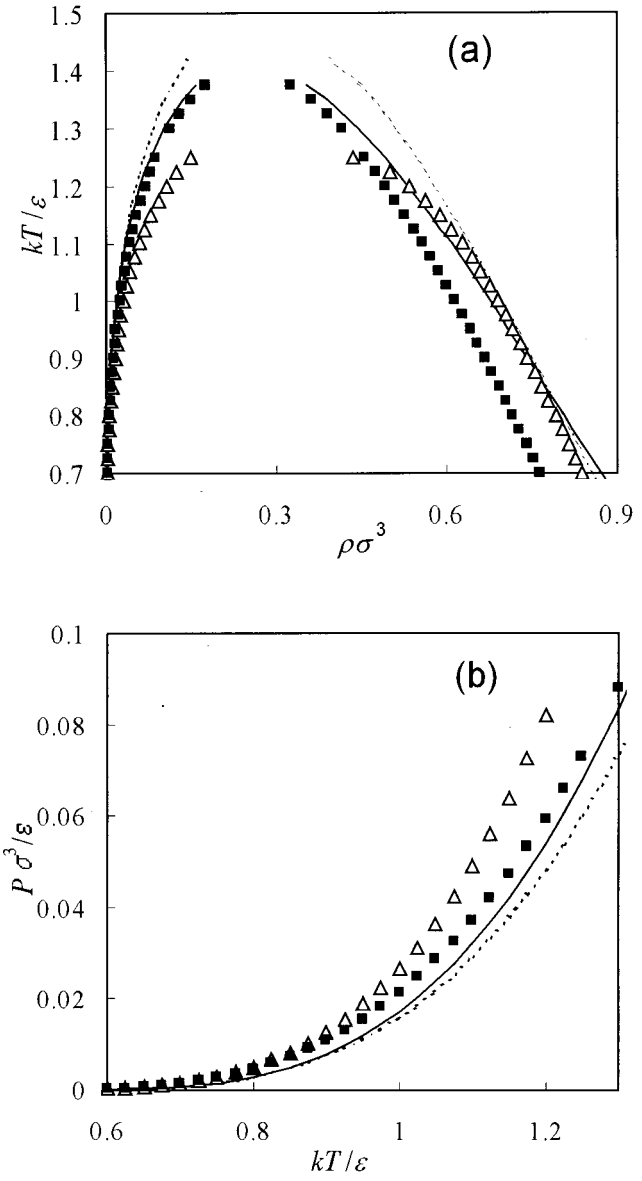

FIG. 2. (a) Vapor-liquid phase envelope and (b) saturated vapor pressure of the $5\sigma_{ff}$ cut LJ fluid. Triangles, LJ equation of state of Johnson *et al.* [84]; squares, mean field DFT using WCA separation and the d_{HS} from the BH formula; dotted line, mean field DFT using WCA separation and d_{HS} according to Lu *et al.* [82] [see Eq. (26)]; solid line, WCA separation using constant $d_{\mathrm{HS}}=\sigma_{ff}$.

shows bulk phase envelopes and saturation pressures for the $5\sigma_{ff}$ cut-and-not-shifted LJ fluid in comparison with the corresponding DFT calculations using WCA [67] division for attractive interactions. We tested several options for the hard-sphere diameter d_{HS}: (1) $d_{\mathrm{HS}}=\sigma_{ff}$ for all temperatures; (2) d_{HS} is taken according to the BH formula [68]; (3) d_{HS} is temperature dependent according to the prescription of Lu *et al.* [82] [Eq. (26)]. The data for the LJ fluid were calculated using equation of state of Johnson *et al.* [84].

It is clear from Fig. 2 that none of the versions of DFT considered is able to describe accurately the vapor-liquid coexistence of a bulk LJ fluid. It is fairly difficult to reproduce both equilibrium liquid density and saturation pressure. The use of the Barker-Henderson relation allows one to reproduce the vapor density and the saturated pressure well, yet severely underestimates the liquid density. On the other hand, when d_{HS} is equal to σ_{ff} or determined according to Lu *et al.* [82], the agreement with the liquid density of the LJ fluid improves substantially, but the vapor density and the pressure are underestimated. All the versions of DFT overestimate the critical temperature. Application of different equations of state for hard spheres leads to only minor differences in the bulk properties.

Discrepancies in prediction of the bulk properties, first of all in the density of the liquid and the saturation pressure, make it problematic to obtain consistent results in molecular simulations and NLDFT using the same fluid-fluid parameters in different models. Moreover, this may lead to substantial systematic error when NLDFT isotherms are directly compared to the experimental data, e.g., for calculation of pore size distributions.

We have obtained the parameters of NLDFT and MC models by fitting the corresponding bulk equations of state to the experimental data on the vapor-liquid equilibrium for a given fluid, namely, the equilibrium gas and liquid densities, and the saturation vapor pressure. Parameters were determined for N_2 and CO_2 as relevant adsorbates in practice. In the DFT, we used an explicit mean field approximation for the attractive interactions with the WCA separation, and the diameter of hard spheres $d_{\mathrm{HS}}=\sigma_{ff}$. We used the CS equation for the hard spheres [75]. The same parameters were used in the NLDFT calculations performed with the SDA [1,4] and FMT [6,7] functionals, thus neglecting the minor differences between the CS and PY representations of the bulk hard-sphere fluids. Applicability of the mean field equation of state to real fluids is generally limited to regions away from the critical point. Thus, no attempt was made to fit the experimental phase diagrams based on the critical temperature. Instead, the parameters of the LJ potentials were obtained by fitting the experimental bulk properties of N_2 [90,91] within a range of temperatures, which included the temperatures of experimental adsorption measurements (normal boiling points of both gases). The procedure for the determination of parameters for N_2 and Ar is described in detail in Ref. [56]. To fit the parameters of the MC model, the LJ fluid equation of state derived by Johnson *et al.* [84] was used. For both the DFT and MC models the attractive potential was cut at $5\sigma_{ff}$.

In Fig. 3 we present the results for the bulk equilibrium for nitrogen. With the parameters found for intermolecular interactions, both NLDFT and MC models represent quite well the properties of the bulk fluid at low temperatures. NLDFT describes the liquid-vapor densities and saturation pressures of N_2 to within 5% accuracy in the interval from the triple point 63 K to ca. 90 K, i.e., from $k_BT/\epsilon_{ff}=0.67$ to 0.95 [Fig. 3(c)]. Bulk equilibrium for CO_2 is described in Ref. [57]. LJ parameters and diameters of hard spheres for all fluids considered are given in Table I.

C. Surface tension of the liquid-vapor interface

Correct prediction of the surface tension is a necessary condition for any model claiming a quantitative description

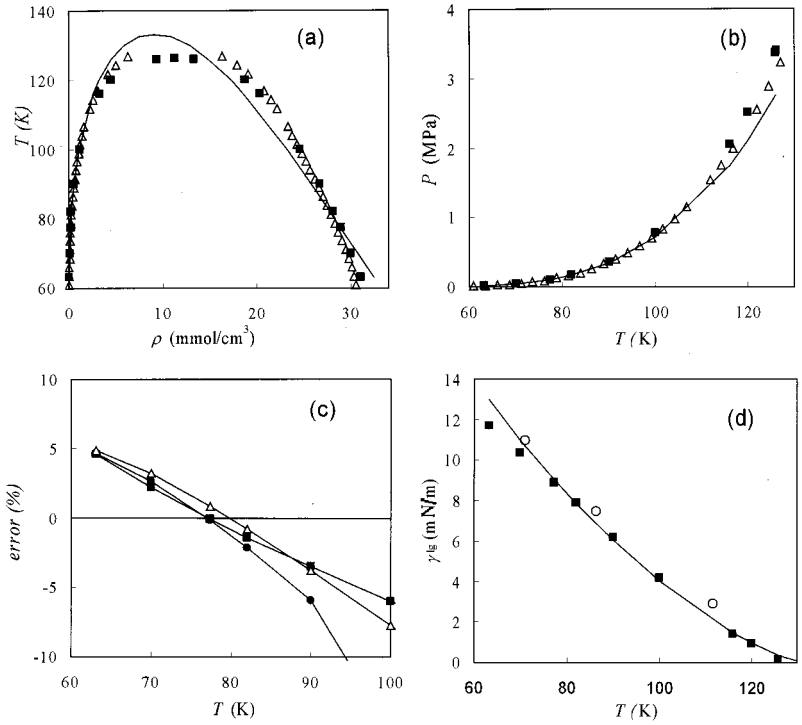

FIG. 3. Prediction of the bulk vapor-liquid equilibrium for LJ nitrogen by the DFT and simulations. (a) Densities of coexisting vapor and liquid phases; (b) saturation pressure. Triangles, LJ model (calculated using equation of state of Johnson *et al.* [84]); solid line, mean field DFT using WCA separation and $d_{\mathrm{HS}}=\sigma_{ff}$ (parameters in Table I); squares, experimental data [90]. (c) Deviations in the DFT predictions of the experimental liquid density (squares), vapor density (circles), and saturation pressure (triangles). (d) Liquid-vapor surface tension. Solid line, mean field DFT calculations using WCA separation and $d_{\mathrm{HS}}=\sigma_{ff}$; squares, experimental data [92]; circles, molecular dynamics simulations of Mecke, Winkelmann, and Fischer [93].

of vapor-liquid transitions in pores. Therefore, we checked that both the NLDFT and MC models give reasonable predictions of the experimental surface tension. In NLDFT, the surface tension of the liquid-vapor interface was calculated as the excess grand potential of the system

$$\gamma_{1g}=(\Omega+P_0V)/A=\Omega/A+P_0H, \tag{34}$$

where A is the area of the interface and P_0 is the equilibrium bulk pressure. Calculations were performed in planar symmetry using a box of $H\approx(30-100)\sigma_{ff}$ width. The calculated surface tension of nitrogen at 77.4 K is only 1.5% greater than the experimental value [Fig. 3(d)]. Surprisingly, the agreement with the experimental data [92] is good even for temperatures close to the critical temperature. For comparison, we show on the same plot the molecular dynamics data of Mecke, Winkelmann, and Fischer [93], calculated with the LJ potential truncated at $5\sigma_{ff}$. It is seen that the agreement among the NLDFT, simulation, and experimental data is good [Fig. 3(d)].

D. Adsorption on open surfaces: Solid-fluid interaction parameters

The same solid-fluid parameters were employed in the NLDFT and MC models. Thus, the adsorption isotherms calculated with different models necessarily coincide in the Henry region. Parameters of nitrogen-carbon interactions were taken as determined by Lastoskie, Gubbins, and Quirke [36]. Parameters of nitrogen-silica interactions were determined by Ravikovitch, Haller, and Neimark from the fit of the experimental data in the multilayer adsorption region [55].

1. Nitrogen on graphite

At subcritical temperatures, adsorption in mesopores proceeds via the formation of a condensed monolayer of the adsorbed fluid on the pore wall(s), followed by the formation of consecutive layers. In sufficiently wide slit pores, interactions between the monolayer films formed on the two opposite walls can be neglected. Thus, the results of the GCMC

TABLE I. Parameters of the intermolecular potentials. Cutoff distance for the fluid-fluid interactions is $5\sigma_{ff}$.

	Fluid-fluid			Solid-fluid			
				Carbon, $\rho_S=0.3819$ Å^{-2}		Silica, $\rho_S=0.153$ Å^{-2}	
Fluid	ϵ_{ff}/k_B (K)	σ_{ff} (Å)	d_{HS} (Å)	ϵ_{sf}/k_B (K)	σ_{sf} (Å)	ϵ_{sf}/k_B (K)	σ_{sf} (Å)
N_2 (DFT)	94.45	3.575	3.575	53.22	3.494	147.3	3.17
(MC)[a]	101.5	3.615		53.22	3.494	147.3	3.17
CO_2 (DFT)	235.9	3.454	3.495	81.5	3.43	147.1	3.30
(MC)	246.2	3.648		81.5	3.43	147.1	3.30
CH_4	148.2	3.82	3.82	64.4	3.60		

[a]Shifted fluid-fluid potential.

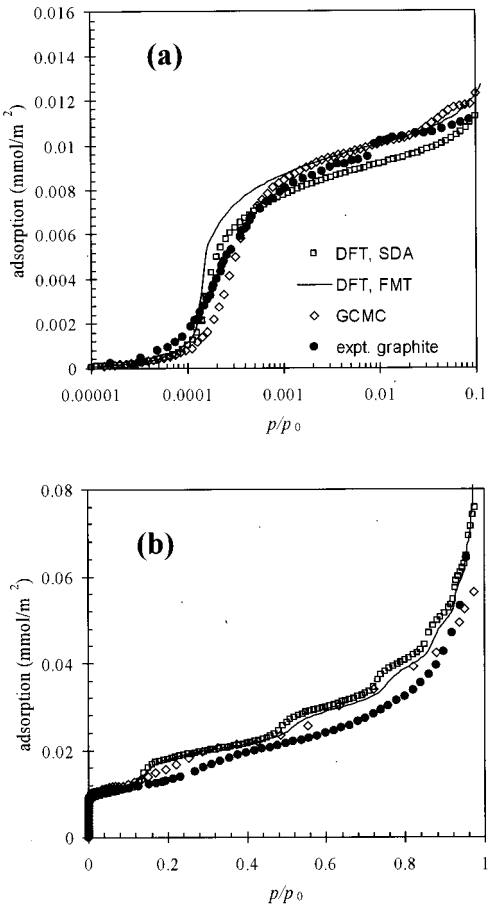

FIG. 4. Isotherm of nitrogen adsorption on graphite at 77.4 K on logarithmic (a) and on linear scale (b). Diamonds, GCMC simulations; solid line, NLDFT calculations using FMT functional; squares, NLDFT calculations using SDA functional; closed circles, experimental isotherm on Sterling graphite [52].

and NLDFT modeling can be directly compared to experimental adsorption isotherms on nonporous graphite. In Fig. 4, we present the calculated adsorption isotherms in the slit carbon pore $H_{CC}=72$ Å $(20\sigma_{ff})$ at pressures well below capillary condensation and the experimental isotherm of nitrogen adsorption on Sterling graphite [52]. The NLDFT and MC models correctly predict the pressure region where the monolayer formation occurs. Nevertheless, some minor disagreement between the theoretical predictions and the experiment has been observed. Both NLDFT models predict steeper monolayer formation than in the experiment. The GCMC simulations yield better agreement with the experiment. The monolayer capacity is predicted well by the simulations and the FMT models, while the SDA underestimates the density of nitrogen monolayers on graphite. A minor step on the experimental isotherm at $p/p_0 \approx 0.01$ corresponds to the incommensurate-commensurate structural transition in the adsorbed monolayer [94]. This transition cannot be described within the spherical model for the nitrogen molecule and the structureless model for the graphite surface, and lies beyond the scope of this work.

As the pressure increases, a multilayer liquidlike film gradually forms on the pore wall. The NLDFT isotherms

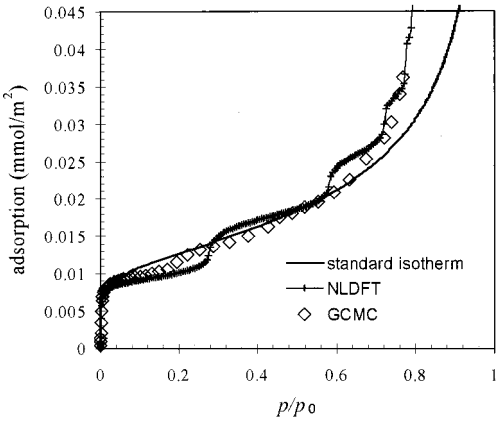

FIG. 5. Nitrogen adsorption isotherms on silica at 77.4 K. Points, GCMC simulations in a 90 Å cylindrical pore; crosses and line, NLDFT calculations in a 90 Å cylindrical pore using SDA functional; solid line, experimental standard adsorption isotherm on nonporous silica [96].

exhibit distinct steps corresponding to the formation of each additional layer [Fig. 4(b)]. These transitions are more pronounced in the SDA model. The GCMC isotherm is smoother. A rounded transition to a two-layer structure can be distinguished on GCMC and experimental isotherms. We should note that theoretical and simulated isotherms show upward deviation from the experimental data at pressures above the monolayer formation pressure: both of them overestimate the thickness or/and density of the liquid film adsorbed on the graphite plane. Similar, even larger deviations were obtained in the NLDFT calculations of Olivier [52]. The author referred this effect to the mean field nature of NLDFT and introduced an empirical weighting function that made it possible to fit the NLDFT isotherm to the experimental data very accurately. However, the fact that the deviations were also obtained in the MC simulations shows that the origin of the disagreement with experimental data should be sought in the simplified model of the fluid-solid interactions. We note that NLDFT adsorption isotherms of Ar on graphite also show similar deviations [52,54], which indicates that they are not specific to N_2, and, therefore, are unlikely to be caused by the deficiencies of the spherical representation of the N_2 molecule. Despite the above mentioned disagreements we conclude that both NLDFT models represent the multilayer adsorption of nitrogen on graphite with the same accuracy as the MC simulations.

2. Nitrogen on silica

The NLDFT and GCMC isotherms were calculated for a siliceous cylindrical pore of 9 nm in diameter using the solid-fluid potential given by Eq. (30). The overall agreement between the NLDFT and GCMC isotherms is good in the whole pressure range; however, as for the isotherm on graphite, the NLDFT predicts more pronounced layering transitions compared to the GCMC isotherm (Fig. 5). As shown by Maddox, Olivier, and Gubbins [95], it is impossible to describe the low-pressure nitrogen adsorption on

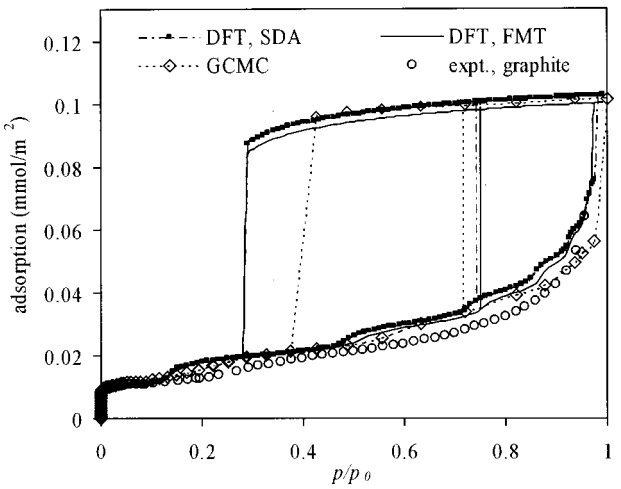

FIG. 6. Nitrogen adsorption isotherms in carbon slit pore $H_{CC}=72$ Å $(20\sigma_{ff})$ at 77.4 K. Diamonds and dotted line, GCMC simulations; solid line, NLDFT calculations using FMT functional; squares and dash-dotted line, NLDFT calculations using SDA functional; open circles, experimental isotherm on Sterling graphite [52]. Vertical lines show locations of spontaneous condensation transition (right), spontaneous desorption (left), and vapor-liquid two-phase coexistence in the pore (middle).

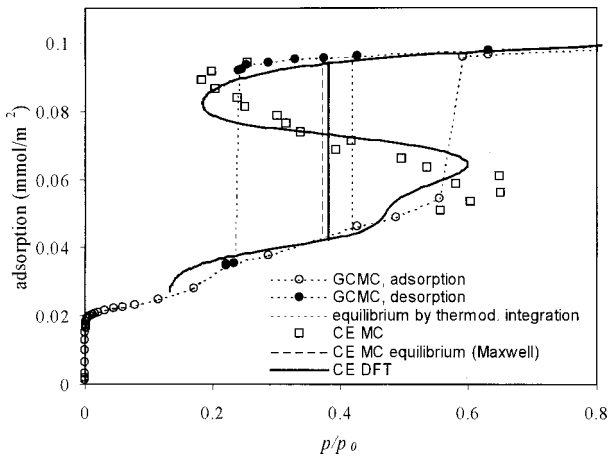

FIG. 7. Nitrogen adsorption isotherms in carbon slit pore $H_{CC}=36$ Å $(10\sigma_{ff})$ at 77.4 K. Open circles and dotted lines, GCMC simulations of the adsorption branch; closed circles and dotted lines, GCMC simulations of the desorption branch; solid line, canonical ensemble NLDFT calculations using SDA functional; open squares, canonical ensemble MC simulations with Widom's insertion method. Dotted vertical lines show locations of spontaneous spinodal condensation transition (right), spontaneous desorption (left), and vapor-liquid two-phase coexistence in the pore calculated by the thermodynamic integration method (middle). Solid and dashed vertical lines correspond to the equilibrium transition pressures calculated using Maxwell rule from CEDFT and CEMC isotherms, respectively.

silica using a structureless model for the surface. The shape of the experimental isotherm of nitrogen sorption to silica at low pressures is affected by substantial geometric and energetic inhomogeneities; therefore, unlike the theoretical ones, the experimental isotherms are smooth and do not exhibit sharp monolayer formation steps [43,53,55,95]. In Fig. 5 we compare the theoretical and simulated isotherms in a 90 Å cylindrical pore with the so-called standard N_2 isotherm on nonporous silica [96]. It is seen that the agreement between the calculated and experimental isotherms is good in the region of multilayer adsorption, at pressures $p/p_0>0.3$. The agreement remains good up to the $p/p_0\sim0.74$, after which the theoretical and simulated isotherms begin to bend upward due to the onset of capillary condensation (Fig. 5). We note that the calculated NLDFT adsorption isotherm in much larger cylindrical pores up to 107 nm in diameter [97] closely follows the experimental standard N_2 isotherm up to pressures of $p/p_0=0.9$ [55,98]. We conclude that the NLDFT and MC models are capable of describing N_2 multilayer adsorption on silica.

E. Vapor-liquid transitions in nanopores

1. Capillary condensation of nitrogen in slit carbon pores

As the pressure increases, the liquid films on the pore walls become unstable and the system exhibits a spinodal transition associated with spontaneous condensation and the formation of a liquidlike state of condensed fluid. For $H_{CC}=72$ Å $(20\sigma_{ff})$ (Fig. 6), both NLDFT models and MC simulations predict the spinodal transition at $p/p_0\approx0.975$, which is well below the saturation pressure of the bulk nitrogen, p_0, and corresponds to the situation of complete wetting of the graphite surface by the adsorbate. The densities of the adsorbed liquid are very similar in the NLDFT models and in the MC simulations, which was expected, as the NLDFT and MC bulk equations of state do not deviate appreciably. Gradually reducing the relative pressure from $p/p_0=1$, we traced equilibrium liquidlike states along the desorption isotherm. The capillary liquid is thermodynamically stable in the pore at pressures above the pressure of vapor-liquid coexistence p_e, and metastable at $p_{sl}<p<p_e$, where p_{sl} is the pressure where spinodal evaporation takes place. The desorption isotherms calculated with the two NLDFT models and GCMC simulations agree well with each other. However, certain differences in the pressure of the spontaneous (spinodal) desorption transition obtained by the GCMC and NLDFT methods are observed. An obvious reason for this difference is the absence of fluctuations in NLDFT. Thus, the metastable desorption branch of the NLDFT isotherms follows all the way up to the spinodal point of the confined liquid. In the GCMC method a spontaneous transition occurs as soon as the free energy barrier between metastable liquid state and thermodynamically stable vapor state at the same μ becomes low enough to be overcome by the density fluctuations allowed in the simulations. As shown in Ref. [87], it is not possible to obtain the true spinodal point in GCMC simulations. In order to test the consistency of the spinodal points in the MC simulations and NLDFT calculations, complete S-shaped adsorption isotherms should be calculated, including stable, metastable, and unstable states with negative compressibility. This can

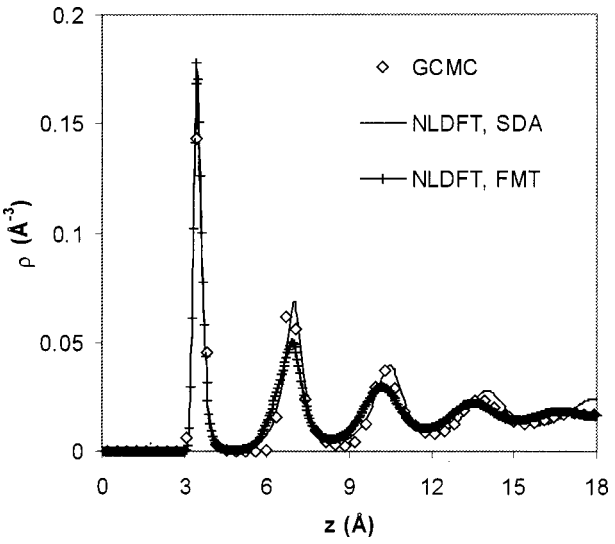

FIG. 8. Density profiles of nitrogen in slit carbon pore $H_{CC}=36$ Å $(10\sigma_{ff})$ at 77.4 K and $p/p_0=0.7$. Points, GCMC simulations; solid line, NLDFT using SDA functional; crosses, NLDFT using FMT functional.

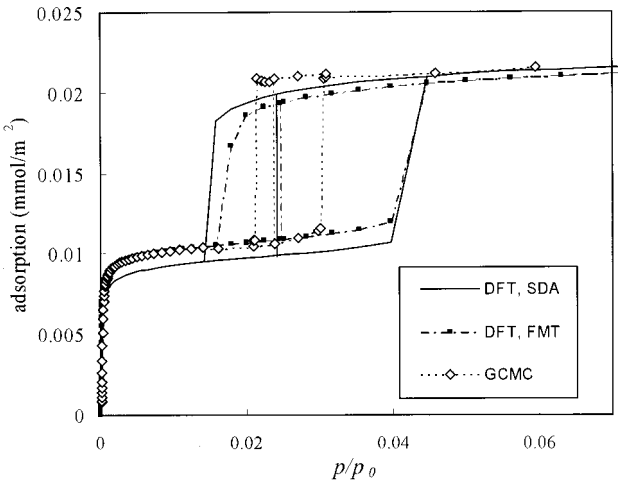

FIG. 9. Nitrogen adsorption isotherms in carbon slit pore $H_{CC}=18$ Å $(5\sigma_{ff})$ at 77.4 K. Diamonds and dotted line, GCMC simulations; solid line, NLDFT calculations using SDA functional; squares and dash-dotted line, NLDFT calculations using FMT functional. Vertical lines show locations of spontaneous condensation transition (right), spontaneous desorption (left), and vapor-liquid two-phase coexistence in the pore (middle).

be done either by the canonical MC simulation (see the example below) or by the gauge cell method [87]. Thin vertical lines on Fig. 6 show the phase coexistence equilibrium pressures predicted by all three models. Good agreement in calculated values of p_c is observed for different models; the discrepancies between the GCMC and NLDFT are within the error of the thermodynamic integration method. Thus, the NLDFT and GCMC data are quantitatively consistent.

We calculated adsorption-desorption isotherms for nitrogen in two smaller slit carbon pores $H_{CC}=36$ $(10\sigma_{ff})$ and 18 Å $(5\sigma_{ff})$. Figure 7 presents the adsorption isotherms in the 36 Å pore $(10\sigma_{ff})$. In this pore three adsorbed layers form on the pore walls before capillary condensation occurs. The GCMC data were complemented by CEMC simulations. The canonical ensemble method allows us to construct the backward trajectory of equilibrium states, which are otherwise unstable in the open system [86]. It should be noted that the error bar for the CEMC points is larger than that for the GCMC points due to intrinsic inaccuracy of the Widom insertion method [65] employed for determination of the chemical potential. The NLDFT isotherm was also calculated in the canonical ensemble by the CEDFT method [46]. From the CEMC and CEDFT isotherms, the location of the vapor-liquid equilibrium is established according to the Maxwell law of equal areas. We also calculated the equilibrium transition pressure using the thermodynamic integration method [85]. The values of the equilibrium pressures estimated by different approaches are in satisfactory agreement with each other and substantially lower compared to those for 72 Å $(20\sigma_{ff})$ pore. This conforms to the established trend that the equilibrium shifts to lower pressures as the pore width decreases.

The structure of the adsorbate in a pore is reflected in the local density profiles. In Fig. 8 we present the density profiles in a condensed fluid in a pore with $H_{CC}=36$ Å $(10\sigma_{ff})$ at $p/p_0=0.7$, which is just above the vapor spinodal pressure. At these conditions the SDA shows nine pronounced adsorbed layers of the adsorbate while GCMC and FMT calculations predict a weaker fluid structuring in the pore center with a tendency to a ten-layer structure. It is worth noting that due to a smaller σ_{ff} (Table I), the ratio of σ_{ff}/H_{CC} in the NLDFT models is slightly lower than that in the GCMC model (Table I). The difference in the fluid structure becomes more pronounced as the pressure increases to p_0.

As the pore width decreases and becomes closer to the capillary critical pore size, the free energy barriers between the metastable and stable states can be more easily overcome by the fluctuations inherent in the GCMC method. This effect is clearly seen in Fig. 9 where we present the NLDFT and GCMC isotherms in the slit pore of $H_{CC}=18$ Å $(H_{CC}=5\sigma_{ff})$. The fluid forms only monolayer films on the pore walls prior to capillary condensation. In this pore, the GCMC generated hysteresis loop is substantially narrower than those obtained by the NLDFT models. However, the location of the equilibrium transition is in very good agreement.

One note should be made regarding different versions of the FMT functional, namely, the RSLT1 and RSLT2 modifications aimed at improved dimensional crossover [Eqs. (19) and (20)] [73,80]. In our calculations of N_2 adsorption in $5\sigma_{ff}$, $10\sigma_{ff}$, and $20\sigma_{ff}$ slit pores we did not find any significant difference between these versions of the FMT functional and the original form [Eq. (18)]. This does not mean that these modifications are not important. We do not consider here situations of extreme confinement, in which the improved functionals are known to perform better (see, e.g., [99]). In our calculations in slit pores, the only noticeable difference between the original and modified FMT functionals was observed at lower temperature, where the fluid attains a solidlike structure (see Sec. III F below).

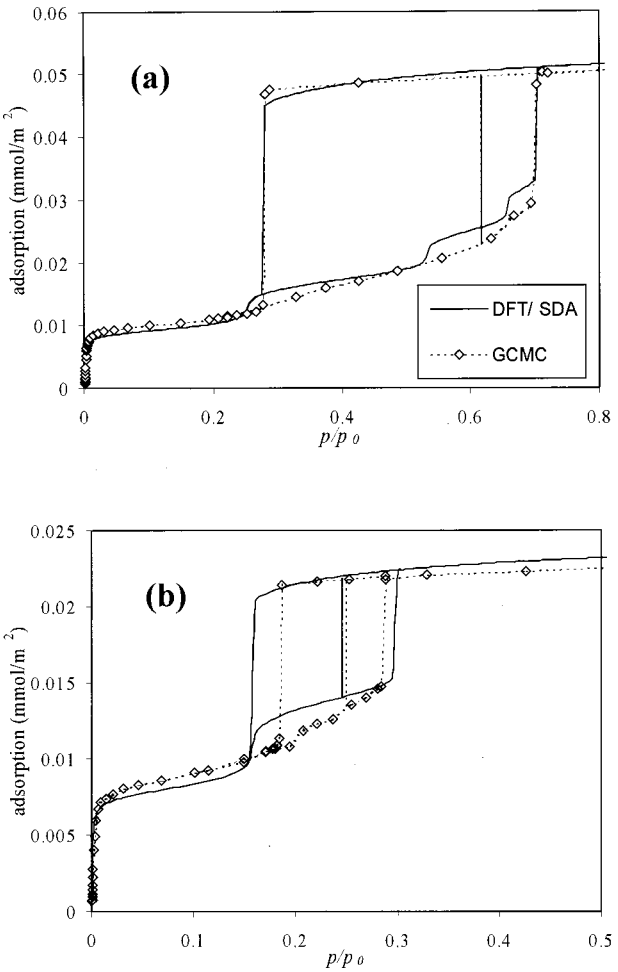

FIG. 10. Nitrogen adsorption isotherms in cylindrical silica pores at 77.4 K. (a) $D_{CC}=72$ Å $(20\sigma_{ff})$; (b) $D_{CC}=36$ Å $(10\sigma_{ff})$. Points and dotted line, GCMC simulations; solid line, NLDFT calculations using SDA functional. Vertical lines show locations of spontaneous condensation transition (right), spontaneous desorption (left), and vapor-liquid two-phase coexistence in the pore (middle).

2. Capillary condensation of nitrogen in cylindrical pores of MCM-41 materials

Following the procedure applied for the slit carbon pores, we estimated the pressures corresponding to the vapor-liquid coexistence as well as the condensation and desorption spinodal transitions in cylindrical pores representing channels in MCM-41 material [94]. For $D_{CC}=72$ Å $(20\sigma_{ff})$, a wide hysteresis loop is obtained [Fig. 10(a)]. Agreement between the NLDFT and GCMC models is excellent. As the pore width decreases, the equilibrium and spinodal points shift toward lower pressures. For $D_{CC}=36$ Å $(10\sigma_{ff})$, both models predict considerable hysteresis, while the hysteresis loop is narrower in the GCMC method [Fig. 10(b)].

Capillary condensation in pores is likely to proceed via formation of density fluctuations along the pore walls; these fluctuations ultimately collapse into a liquid embryo, leading to spontaneous condensation. These fluctuations cannot be taken into account in the NLDFT, which considers only symmetrical solutions for the density profiles inside the pore,

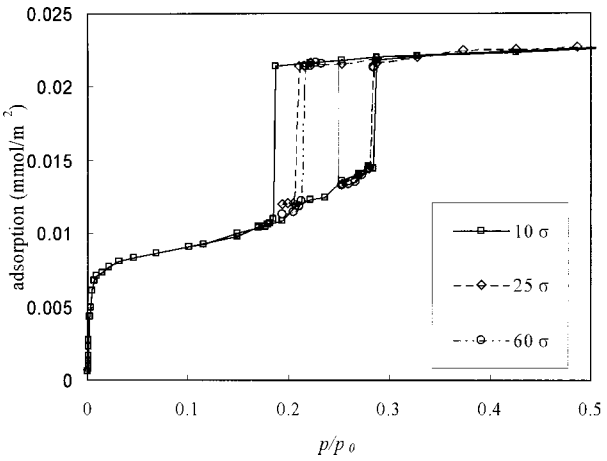

FIG. 11. GCMC nitrogen adsorption isotherms in cylindrical silica pore $D_{CC}=36$ Å $(10\sigma_{ff})$ at 77.4 K, calculated with different length of the simulation cell, $10\sigma_{ff}$, $25\sigma_{ff}$, and $60\sigma_{ff}$.

assuming that the adsorbate is uniform in the direction(s) parallel to the wall(s). In the GCMC method the density fluctuations are restricted by periodic boundary conditions imposed in the directions parallel to the walls. We have checked the influence of finite size effects in GCMC simulations by considering different length of the simulation cell l_z. Figure 11 demonstrates GCMC isotherms in the pore $D_{CC}=36$ Å $(10\sigma_{ff})$ calculated with $l_z=10\sigma_{ff}$, $25\sigma_{ff}$, and $60\sigma_{ff}$. Since the points on stable parts of both vapor and liquid branches of desorption isotherms essentially coincide for different l_z, we cannot expect any substantial shift in the equilibrium transition. As the cell length is increased the point of spontaneous desorption shifts toward the point of equilibrium transition, while the capillary condensation pressure remains unchanged. This supports the classical scenario of capillary condensation hysteresis in open-ended cylindrical pores [100]. In open-ended cylindrical pores, the desorption occurs at the point of equilibrium transition and the condensation occurs spontaneously at the vaporlike spinodal. We have shown recently that the NLDFT and GCMC simulated hysteresis loops formed by the metastable adsorption and equilibrium desorption branches are in perfect agreement with the experimental data on regular materials with cylindrical pores greater than ca. 50 Å [51,98,101–103]. As a typical example we present in Fig. 12 GCMC and NLDFT nitrogen isotherms in comparison with the isotherm on a sample of MCM-41 type material [104] with uniform tubular pores.

As the pore width decreases, the theoretical hysteresis loop narrows and disappears when the pore width critical to the pore vapor-liquid equilibrium is reached. The adsorption becomes supercritical as soon as the pore is able to accommodate only two adsorbed layers on the pore wall [51,87,101]. We have observed certain differences in the critical pore widths predicted by the NLDFT and GCMC models. Figure 13 shows the calculated adsorption isotherms in a pore of $D_{CC}=18$ Å $(5\sigma_{ff})$ in diameter. According to the GCMC method, adsorption in this pore is supercritical: no first-order capillary condensation takes place. Instead, a distinct continuous formation of the second adsorbed layer is

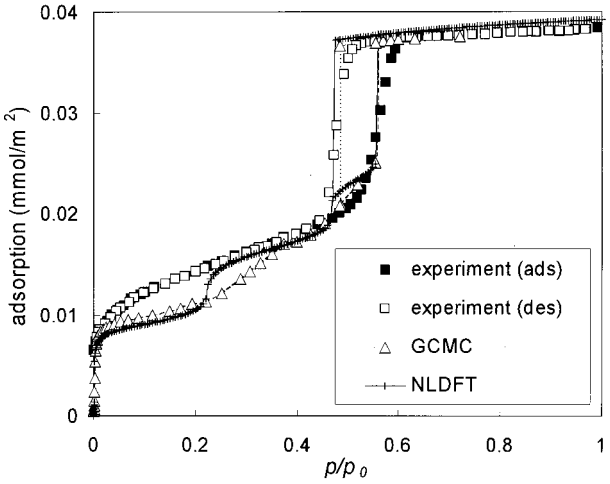

FIG. 12. Nitrogen adsorption-desorption isotherms at 77.4 K in cylindrical pores of $D_{CC}=54$ Å ($14.9\sigma_{ff}$). Triangles, GCMC simulations; line and crosses, NLDFT calculations using SDA functional; squares, experimental isotherm on MCM-41-like material [104].

observed (Fig. 13). The NLDFT predicts a first-order capillary condensation to the two-layer structure. Thus, disagreement between the NLDFT and GCMC simulations becomes more serious in narrow pores. It is worth noting that recent simulations [87] have shown that the GCMC may produce reversible isotherms similar to that displayed in Fig. 13 even at subcritical conditions.

Figure 14 demonstrates the NLDFT and GCMC density profiles in cylindrical pores of $5\sigma_{ff}$, $10\sigma_{ff}$, and $20\sigma_{ff}$ in diameter. It is evident that NLDFT is able to describe the density profiles very accurately in both narrow [Fig. 14(a)] and wide pores [Fig. 14(c)]. In the $10\sigma_{ff}$ pore, the NLDFT and GCMC density profiles agree very well with each other for the first three layers; however, in the pore center, NLDFT

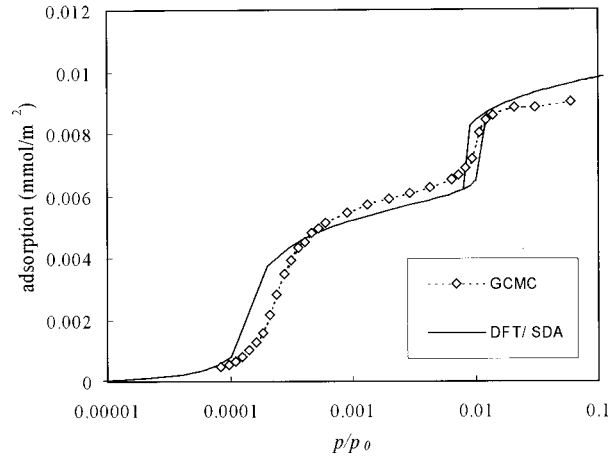

FIG. 13. Nitrogen adsorption isotherms in cylindrical silica pore $D_{CC}=18$ Å ($5\sigma_{ff}$) at 77.4 K. Points, GCMC simulations; solid line, NLDFT calculations using SDA functional. Solid vertical lines show locations of spontaneous condensation transition (right), and spontaneous desorption (left) in the NLDFT calculations.

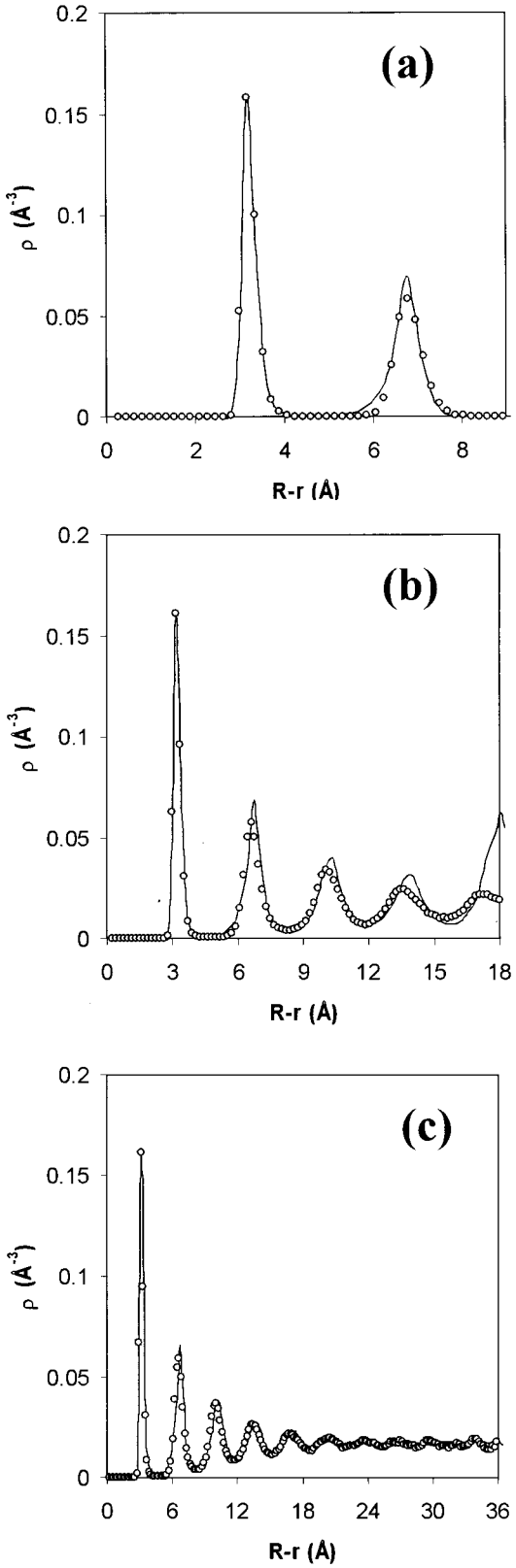

FIG. 14. Density profiles of nitrogen in cylindrical pores at 77 K. Points, GCMC simulations; lines, NLDFT in the SDA approximation. (a) $D_{CC}=18$ Å ($5\sigma_{ff}$) at $P/P_0=0.014$; (b) $D_{CC}=36$ Å ($10\sigma_{ff}$) at $P/P_0=0.38$; (c) $D_{CC}=72$ Å ($20\sigma_{ff}$) at $P/P_0=0.822$.

predicts a sharp peak, in contrast to the GCMC simulation [Fig. 14(b)]. One possible reason for this discrepancy is the radial symmetry of the density profiles imposed in the NLDFT calculations. However, the contribution of the central peak to the total density is small.

F. Freezing of methane in slit pores

In MC simulations, the liquid-solid transition in LJ fluids adsorbed in slit and cylindrical nanopores has been established by a number of criteria, including abrupt changes in density and thermodynamic functions, diffusion coefficients, and structural parameters [105–109]. It was shown that the character and the conditions of the freezing and melting transitions in pores depend on the pore width, the strength of the fluid-solid interactions, and the structure of the solid wall. The NLDFT models that we test in this paper are essentially one dimensional in the sense that they do not consider the molecular structure of the fluid in the directions parallel to the pore wall. Thus, it is impossible to identify the fluid freezing. Nevertheless, it is of general interest to compare the density profiles in the direction perpendicular to the walls, and to check to what extent NLDFT is capable of describing the solidlike structure in slit pores at low temperatures. We tested the SDA and FMT functionals in the conditions corresponding to the freezing of LJ methane in slit pores, established earlier by the GCMC simulations of Vishnyakov, Piotrovskaya, and Brodskaya [105]. We modeled methane in slit pores $H_{CC}=10\sigma_{ff}$ and $8\sigma_{ff}$ at $kT/\epsilon_{ff}=0.75$ (111 K) with the LJ parameters used in the simulations [105], $\sigma_{ff}=3.82$ Å, and $\epsilon_{ff}/k=148.2$ K. The solid-fluid interactions were described by the 10-4-3 potential [88] with the parameters corresponding to methane-graphite interactions.

The GCMC and NLDFT isotherms of methane at 111 K in $8\sigma_{ff}$ and $10\sigma_{ff}$ carbon pores exhibit a capillary condensation step accompanied by a hysteresis loop. The positions of the equilibrium transition are in reasonable agreement. In the $8\sigma_{ff}$ pore the NLDFT predicts equilibrium capillary condensation at $\mu/\epsilon_{ff}=-10.5$, while in simulations it was estimated as $\mu/\epsilon_{ff}=-10.62$ [105]. Figure 15(a) shows density profiles of methane in the $10\sigma_{ff}$ pore after capillary condensation. In these conditions, the pore fluid is liquidlike; the density profile has ten pronounced layers. The FMT functional in its original (we used here the Kierlik-Rosinberg weighting functions [7]) and modified versions (RSLT2) [73] describes the density profile very well, while the SDA functional [4] predicts only nine adsorbed layers [Fig. 15(a)]. With further increase in pressure, the GCMC simulations predict a first-order freezing transition in both $8\sigma_{ff}$ and $10\sigma_{ff}$ pores [105]. Neither of the NLDFT calculations showed a sign of the transition; instead the fluid density in the pore increased continuously. In the $10\sigma_{ff}$ pore, the density profiles predicted by the SDA functional exhibit a gradual structural transformation from the nine- to a ten-layer solidlike structure. An unexpected result is that the solidlike density profile obtained by the SDA theory represents very well the profile predicted by the GCMC simulations, while the FMT underestimates the fluid structuring. A similar picture was observed in the $H_{CC}=8\sigma_{ff}$ pore. Figure 15(b) shows how well the SDA describes the density profiles for a high-density solidlike state of the pore fluid. In contrast, the FMT functionals significantly underestimate the fluid structuring in the pore. Essentially the same qualitative result was obtained using different modifications of the FMT model (RSLT2 and RSLT1, $q=3$) [Fig. 15(b)]. These peculiar observations require additional studies.

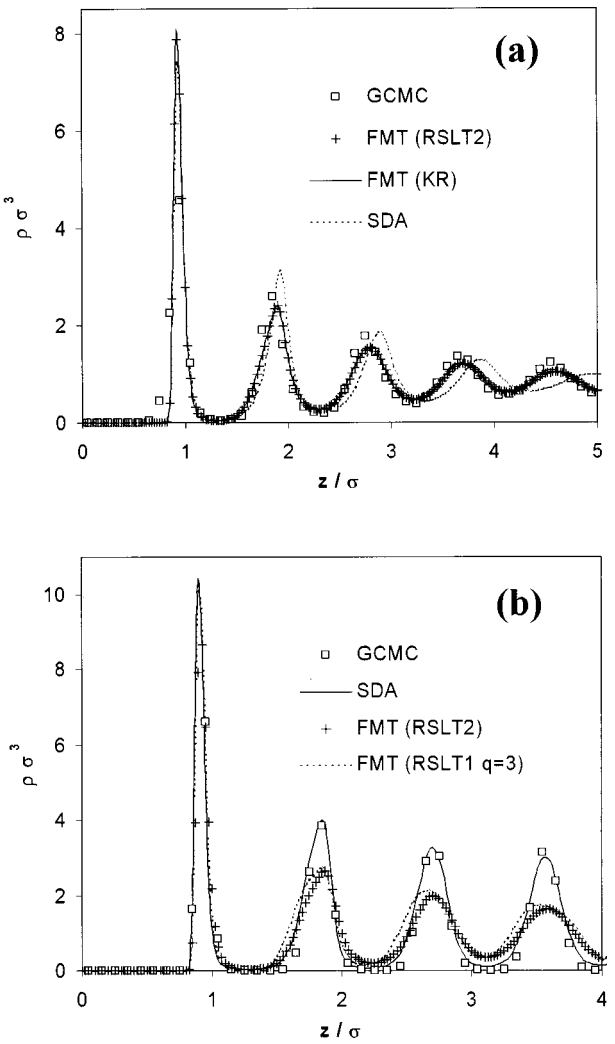

FIG. 15. Density profiles of methane in carbon slit pores at 111 K. (a) Liquidlike structure in an $H_{CC}=8\sigma_{ff}$ pore: points, GCMC simulations [105]; solid line, FMT functional in the KR version [7]; crosses, modified FMT functional; dotted line, SDA functional. (b) Solidlike structure in an $H_{CC}=10\sigma_{ff}$ pore: points, GCMC simulations [105]; solid line, SDA functional; crosses and dotted line, modified versions of the FMT functional.

G. CO_2 adsorption in one-dimensional cylindrical micropores

In this section we consider adsorption in pores in which the attractive adsorption fields from opposite walls interfere, so that the adsorption potential forms a single minimum at the pore center, which is typical for many zeolites. Such pores are able to accommodate only a single file of the adsorbate particles, i.e., the fluid approaches the one-dimensional limit. It is known that the SDA functional [1,4]

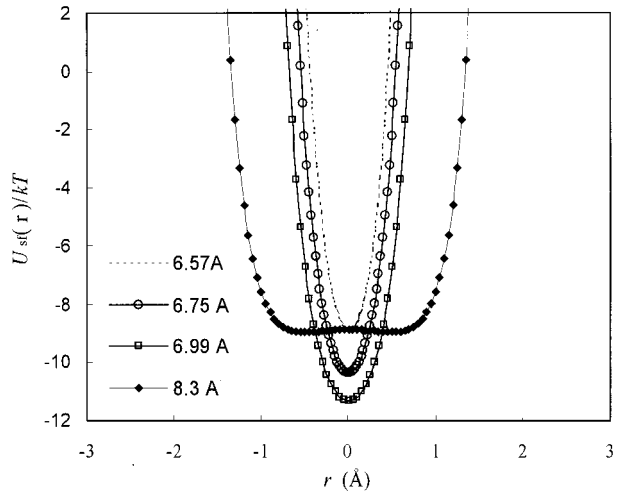

FIG. 16. Solid-fluid potential for CO_2 in cylindrical micropores of different widths (as shown in the legend). r denotes the distance from the pore axis.

does not give the correct one-dimensional limit [73]; therefore it is of interest to find the lower limit of applicability of the three-dimensional SDA functional in very narrow cylindrical pores. As a practical example, we considered a LJ fluid with interaction parameters chosen to model CO_2 adsorption at 273.2 K in cylindrical pores of $D_{CC}=8.3$, 6.99, 6.75, 6.57, and 6.22 Å width ($D_{CC}=2.40\sigma_{ff}$, $2.02\sigma_{ff}$, $1.95\sigma_{ff}$, $1.90\sigma_{ff}$, and $1.80\sigma_{ff}$, respectively). Figure 16 shows the fluid-solid potential for CO_2 in these pores calculated by Eq. (30). In the widest pore, $D_{CC}=8.3$ Å ($2.4\sigma_{ff}$), which can be considered as a crude model for the MFI type of zeolite [94], the potential has two shallow minima. The parameters of CO_2-wall interactions were chosen to reproduce the experimental isotherms of CO_2 on this type of zeolite [110]. In narrower pores the potential has only a single minimum (Fig. 16). As the pore size decreases the potential well first increases, and then the repulsive contributions from the opposite walls start to interfere, leading to a decrease in the attractive wall-fluid interactions. Among the systems considered the pore $D_{CC}=6.99$ Å ($D_{CC}=2.02\sigma_{ff}$) has the deepest energy minimum.

Figure 17 shows the GCMC and NLDFT isotherms in cylindrical micropores. The parameters of the LJ potential, fitted to the bulk properties of CO_2, were taken from our previous work [54,57]. Two series of GCMC isotherms were calculated with different sets of the fluid-fluid LJ parameters, optimized for GCMC simulations and optimized for NLDFT, since it is not clear that the parameters chosen to describe the experimental data for the macroscopic three-dimensional system would be suitable at the one-dimensional limit. The NLDFT isotherm agrees well with the GCMC isotherm, cal-

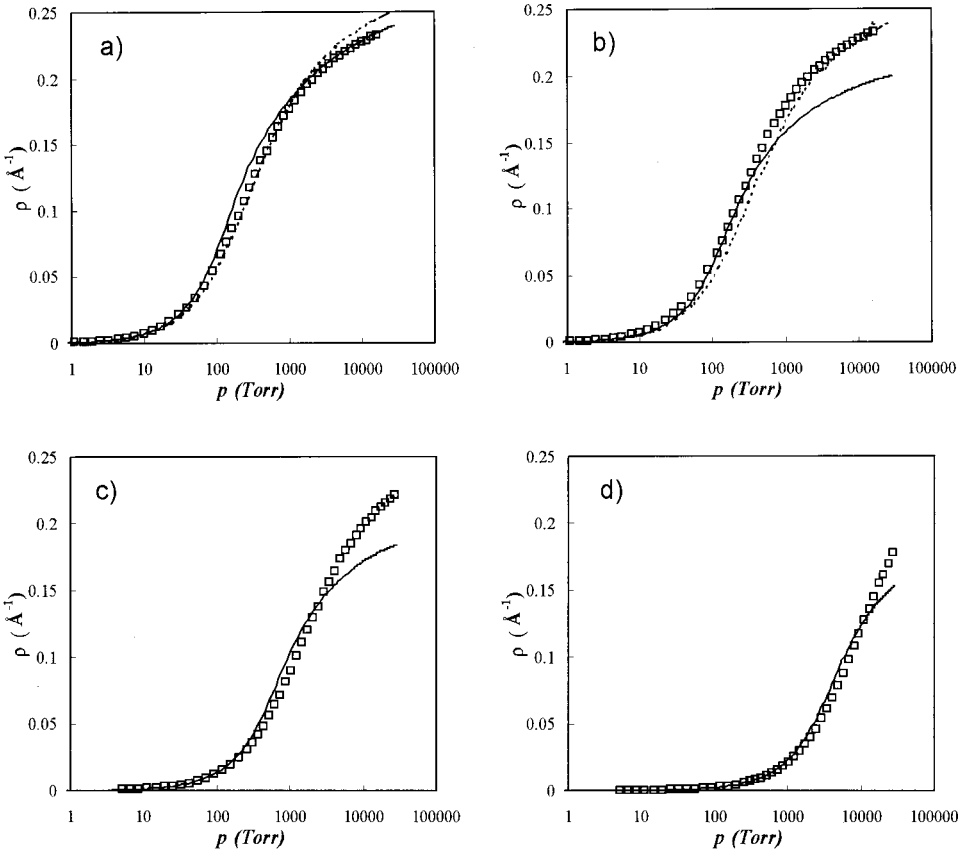

FIG. 17. CO_2 adsorption isotherms at 273.2 K ($kT/\epsilon_{ff}=1.15$) in cylindrical micropores of $D_{CC}=8.3$ Å $=2.4\sigma_{ff}$ (a); 6.99 Å $=2.02\sigma_{ff}$ (b); 6.75 Å $=1.95\sigma_{ff}$ (c); and 6.75 Å $=1.9\sigma_{ff}$ (d). Squares, GCMC simulations with the parameters optimized to descibe bulk CO_2; solid line, NLDFT calculations using SDA functional; dashed line, GCMC simulations with the same LJ parameters as in the NLDFT model.

culated with the LJ parameters optimized for bulk CO_2 [Fig. 17(a)]. Due to the slightly smaller molecular diameter used, the GCMC simulation yields slightly denser packing of molecules in the pore. Good agreement between simulations and NLDFT was also obtained when simulations were performed with the parameters optimized for NLDFT. The SDA model behaves surprisingly well in this pore [Fig. 17(a)]. In the narrower pores, $D_{CC}=6.99$ Å $(2.02\sigma_{ff})$, 6.75 Å $(1.95\sigma_{ff})$, and 6.57 Å $(1.9\sigma_{ff})$, appreciable discrepancies between the NLDFT and GCMC isotherms are seen at high pressures [Figs. 17(b)–17(d)].

We compared our calculations with a rigorous result for the one-dimensional LJ fluid in an external field [44,111]. For this system one can write that

$$\ln(\rho K_H/L)=-\ln\left(\int_0^\infty e^{-[u(z)+\pi z]/kT}dz\right). \tag{35}$$

Here p is the bulk pressure, L is the system length, $u(z)$ is the LJ potential of interactions between particles along the pore axis, π is the one-dimensional pressure, and K_H is the Henry constant determined by the solid-fluid potential $u_{sf}(r)$. In cylindrical pores

$$K_H/L=\frac{2\pi}{kT}\int_0^R r\,dr(e^{-u_{sf}(r)/kT}-1). \tag{36}$$

Adsorption per unit length of the pore is given by

$$\frac{N_a}{L}=\frac{\int_0^\infty e^{-[u(z)+\pi z]/kT}dz}{\int_0^\infty z e^{-[u(z)+\pi z]/kT}dz}. \tag{37}$$

By evaluating Eqs. (35) and (37) for given values of π, one obtains the adsorption isotherm in the form of N_a/L as a function of $\ln(pK_H/L)$.

In Fig. 18 we compare the NLDFT and GCMC isotherms in rescaled form with the isotherm for the one-dimensional LJ fluid. In the GCMC simulations the LJ fluid behaved as a one-dimensional one in all pores except for the largest, $D_{CC}=8.3$ Å $(2.40\sigma_{ff})$, which can accommodate more molecules at high pressures [Fig. 18(a)]. In contrast, the SDA underestimates the density at high pressures, especially in the narrowest pores [Fig. 18(b)].

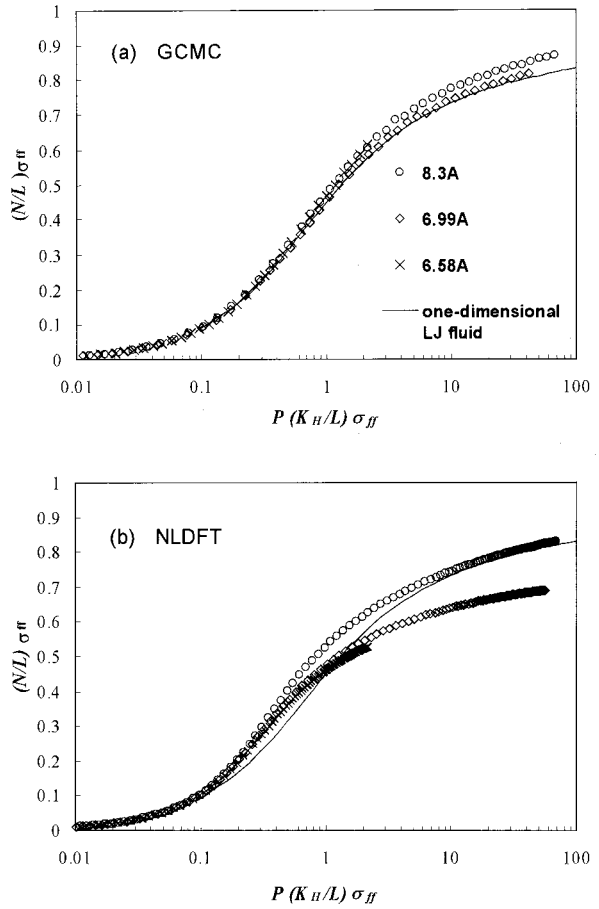

FIG. 18. GCMC (a) and NLDFT (b) isotherms of CO_2 adsorption in cylindrical micropores at 273.2 K in dimensionless rescaled form. Pore widths shown in the legend. Solid line shows the solution for the one-dimensional LJ fluid [111].

IV. SUMMARY AND CONCLUSIONS

In this work we have systematically tested the nonlocal density functional theory of confined fluids against benchmark MC simulations. We modeled LJ fluids in slit-shaped and cylindrical pores. The interaction parameters were chosen to imitate systems important in practice: nitrogen at 77.4 K in slit-shaped carbon pores and cylindrical silica pores, CO_2 at 273 K in cylindrical micropores of zeolites, and methane at 111 K in carbon slit-shaped pores. Two versions of NLDFT were used, the smoothed density approximation and the fundamental measure theory.

First of all, we tested the SDA and FMT density functionals against the benchmark GCMC results [9] and found good agreement for the density profiles of a hard-sphere fluid at an attractive wall (Fig. 1). After that, we compared the LJ fluid bulk phase diagrams for the DFT and MC models (Fig. 2). It was found that it is not possible to achieve quantitative agreement between the MC and DFT phase diagrams. Differences in the bulk phase diagrams cause ambiguities in the comparison of theoretical and simulated results, and lead to serious discrepancies between the MC and NLDFT adsorption isotherms in pores. To remedy this situation, we determined two sets of parameters for fluid-fluid intermolecular interactions by separately fitting the DFT and simulated phase diagrams for the bulk fluid to experimental data on vapor-liquid equilibrium for the system of interest (Fig. 3). That is, we used in the studies of confined fluids different fluid-fluid interaction parameters for the DFT and MC models to provide for the consistent description of the bulk phases. This approach to parameter fitting gave good agreement among the NLDFT, simulated, and experimental data for the surface tension of the liquid-vapor interface for nitrogen at 70–120 K. The solid-fluid parameters were chosen to reproduce experimental adsorption isotherms on nonporous graphite and silica surfaces and were the same in the DFT and MC models (Figs. 4 and 5).

By using this parametrization, we obtained good agreement between the NLDFT and MC nitrogen adsorption-desorption isotherms in slit-shaped and cylindrical mesopores at 77.4 K (Figs. 6–13). Both NLDFT and MC modeling were performed in the grand canonical and canonical ensembles. The conditions of vapor-liquid coexistence in pores were determined from the equality of the grand potentials of vaporlike and liquidlike phases. Two methods of determination of phase coexistence from MC simulations were applied: (1) thermodynamic integration according to the Peterson-Gubbins scheme; (2) integration along the full sigmoid adsorption isotherm, which includes thermodynamically stable, metastable, and unstable states. The chemical potential of the fluid in the canonical ensemble MC simulations was determined using the Widom particle insertion method. In most of the examples considered, we found excellent agreement between the vapor-liquid equilibrium pressures calculated by the NLDFT and the MC simulations.

Nitrogen isotherms in cylindrical pores were compared with the experimental isotherms in siliceous MCM-41 type materials with tubular pores. We found quantitative agreement for pores larger than ca. 5 nm, or 14 molecular diameters in width (Fig. 12). In these pores, capillary condensation occurs at the point of spinodal transition from the adsorbed film to a liquidlike condensed fluid while desorption occurs at the point of equilibrium transition. In smaller pores, both NLDFT and MC models describe quantitatively the pressures of equilibrium transitions. However, they predict higher pressures of capillary condensation than the experimentally observed ones and, correspondingly, wider hysteresis loops, in contrast to the numerous experimental observations indicating that N_2 hysteresis at 77 K is not observed at relative pressures below ca. 0.42 [112,94]. This issue is beyond the scope of this paper. It is also worth noting that in all pores the NLDFT models show larger compressibility compared to GCMC simulations.

The ability of the NLDFT to predict the fluid structure of a solidlike phase was tested by using methane sorption at 111 K in slit-shaped carbon pores. As expected, NLDFT does not reproduce the freezing transition in pores, as does the simulation. Instead, the fluid density increases continuously with pressure. However, at densities corresponding to solidlike methane in pores, the SDA theory shows solidlike density profiles, which are in very good agreement with GCMC results [105] (Fig. 15). In contrast, the FMT functionals underestimate the fluid structuring in these conditions.

To test the SDA functional in the vicinity of the one-dimensional limit, we considered a LJ fluid with parameters chosen to represent CO_2 at 273.2 K in narrow cylindrical pores resembling zeolite channels. In general, the SDA and MC isotherms show quantitative agreement in all but the narrowest pores. While the NLDFT performs well in a pore of diameter $D_{cc}=8.3$ Å, serious discrepancies with GCMC simulations were found in the narrowest pores, which are able to accommodate only one file of molecules (Fig. 17). NLDFT substantially underestimates the fluid density in pores for which the GCMC isotherm in dimensionless rescaled units essentially merges with the rigorous result for the confined one-dimensional LJ fluid.

The comparison with benchmark MC simulations and reference experiments allows us to make a general conclusion: Within reasonable limits, NLDFT with properly chosen parameters of intermolecular interactions is capable of quantitatively predicting the confined fluid structure at solid surfaces and in pores, adsorption isotherms, and conditions of phase equilibrium and spinodal transitions.

ACKNOWLEDGMENTS

This work was supported by the TRI/Princeton exploratory research program and EPA Grant No. R825959-010. We thank E. Kierlik and M. Rosinberg for sharing their original FMT code.

[1] P. Tarazona, Phys. Rev. A **31**, 2672 (1985).
[2] W. A. Curtin and N. W. Ashcroft, Phys. Rev. A **32**, 2909 (1985).
[3] T. F. Meister and D. M. Kroll, Phys. Rev. A **31**, 4055 (1985).
[4] P. Tarazona, U. M. B. Marconi, and R. Evans, Mol. Phys. **60**, 573 (1987).
[5] A. R. Denton and N. W. Ashcroft, Phys. Rev. A **39**, 4701 (1989).
[6] Y. Rosenfeld, Phys. Rev. Lett. **63**, 980 (1989).
[7] E. Kierlik and M. L. Rosinberg, Phys. Rev. A **42**, 3382 (1990).
[8] R. Evans, in *Fundamentals of Inhomogeneous Fluids*, edited by D. Henderson (Marcel Dekker, New York, 1992), Chap. 5.
[9] S. Sokolowski and J. Fischer, Mol. Phys. **68**, 647 (1989).
[10] S. Sokolowski and J. Fischer, J. Chem. Soc., Faraday Trans. **89**, 789 (1993).
[11] S. C. Kim, M. Calleja, and G. Rickayzen, J. Phys.: Condens. Matter **7**, 8053 (1995).
[12] S. C. Kim, J. Phys.: Condens. Matter **8**, 959 (1996).
[13] T. H. Yoon and S. C. Kim, Phys. Rev. E **58**, 4541 (1998).
[14] S. Q. Zhou and E. Ruckenstein, J. Chem. Phys. **112**, 8079 (2000).
[15] J. G. Powles, G. Rickayzen, and M. L. Williams, Mol. Phys. **64**, 33 (1988).
[16] T. K. Vanderlick, L. E. Scriven, and H. T. Davis, J. Chem. Phys. **90**, 2422 (1989).
[17] R. Leidl and H. Wagner, J. Chem. Phys. **98**, 4142 (1993).
[18] P. B. Balbuena and K. E. Gubbins, Langmuir **9**, 1801 (1993).
[19] B. K. Peterson, G. S. Heffelfinger, K. E. Gubbins, and F. van Swol, J. Chem. Phys. **93**, 679 (1990).
[20] B. K. Peterson, K. E. Gubbins, G. S. Heffelfinger, U. Marini, B. Marconi, and F. van Swol, J. Chem. Phys. **88**, 6487 (1988).

[21] N. Choudhury and S. K. Ghosh, J. Chem. Phys. **111**, 1737 (1999).
[22] M. Calleja, A. N. North, J. G. Powles, and G. Rickayzen, Mol. Phys. **73**, 973 (1991).
[23] D. Henderson and S. Sokolowski, Phys. Rev. E **52**, 758 (1995).
[24] A. Gonzalez, J. A. White, F. L. Roman, S. Velasco, and R. Evans, Phys. Rev. Lett. **79**, 2466 (1997).
[25] R. Evans, U. M. B. Marconi, and P. Tarazona, J. Chem. Soc., Faraday Trans. 2 **82**, 1763 (1986).
[26] B. K. Peterson, J. Walton, and K. E. Gubbins, J. Chem. Soc., Faraday Trans. 2 **82**, 1789 (1986).
[27] P. C. Ball and R. Evans, J. Chem. Phys. **89**, 4412 (1988).
[28] P. C. Ball and R. Evans, Langmuir **5**, 714 (1989).
[29] Z. M. Tan, U. M. B. Marconi, F. van Swol, and K. E. Gubbins, J. Chem. Phys. **90**, 3704 (1989).
[30] R. Evans, J. Phys.: Condens. Matter **2**, 8989 (1990).
[31] S. Sokolowski and J. Fischer, Mol. Phys. **71**, 393 (1990).
[32] F. van Swol and J. R. Henderson, Phys. Rev. A **43**, 2932 (1991).
[33] E. Kierlik and M. L. Rosinberg, Phys. Rev. A **44**, 5025 (1991).
[34] E. Kozak and S. Sokolowski, J. Chem. Soc., Faraday Trans. **87**, 3415 (1991).
[35] E. Kierlik, M. Rosinberg, J. E. Finn, and P. A. Monson, Mol. Phys. **75**, 1435 (1992).
[36] C. Lastoskie, K. E. Gubbins, and N. Quirke, J. Phys. Chem. **97**, 4786 (1993).
[37] C. Lastoskie, K. E. Gubbins, and N. Quirke, Langmuir **9**, 2693 (1993).
[38] E. Kierlik, M. L. Rosinberg, Y. Fan, and P. A. Monson, J. Chem. Phys. **101**, 10947 (1994).
[39] E. Kozak, G. Chmiel, A. Patrykiejew, and S. Sokolowski, Phys. Lett. A **189**, 94 (1994).
[40] C. Chmiel, K. Karykowski, A. Patrykiejew, W. Rzysko, and S. Sokolowski, Mol. Phys. **81**, 691 (1994).
[41] E. Kierlik, Y. Fan, P. A. Monson, and M. L. Rosinberg, J. Chem. Phys. **102**, 3712 (1995).
[42] S. Phan, E. Kierlik, M. L. Rosinberg, A. Yethiraj, and R. Dickman, J. Chem. Phys. **102**, 2141 (1995).
[43] P. I. Ravikovitch, S. C. O'Domhnaill, A. V. Neimark, F. Schuth, and K. K. Unger, Langmuir **11**, 4765 (1995).
[44] H. T. Davis, *Statistical Mechanics of Phases, Interfaces, and Thin Films* (Wiley-VCH, New York, 1996).
[45] A. V. Neimark and P. I. Ravikovitch, Langmuir **13**, 5148 (1997).
[46] A. V. Neimark and P. I. Ravikovitch, in *Microscopic Simulation of Interfacial Phenomena in Solids and Liquids*, edited by S. R. Phillpot *et al.*, Mater. Res. Soc. Symp. Proc. 492 (Materials Research Society, Warrendale, PA, 1998), 47.
[47] C. M. Lastoskie, N. Quirke, and K. E. Gubbins, Stud. Surf. Sci. Catal. **104**, 745 (1997).
[48] T. Wadewitz and J. Winkelmann, Phys. Chem. Chem. Phys. **1**, 3335 (1999).
[49] L. J. D. Frink and A. G. Salinger, J. Chem. Phys. **110**, 5969 (1999).
[50] L. D. Gelb, K. E. Gubbins, R. Radhakrishnan, and M. Sliwinska-Bartkowiak, Rep. Prog. Phys. **62**, 1573 (1999).
[51] A. V. Neimark, P. I. Ravikovitch, and A. Vishnyakov, Phys. Rev. E **62**, R1493 (2000).
[52] J. P. Olivier, J. Porous Mater. **2**, 217 (1995).
[53] P. I. Ravikovitch, D. Wei, W. T. Chueh, G. L. Haller, and A. V. Neimark, J. Phys. Chem. B **101**, 3671 (1997).
[54] P. I. Ravikovitch, A. Vishnyakov, R. Russo, and A. V. Neimark, Langmuir **16**, 2311 (2000).
[55] P. I. Ravikovitch, G. L. Haller, and A. V. Neimark, Adv. Colloid Interface Sci. **77**, 203 (1998).
[56] A. V. Neimark, P. I. Ravikovitch, M. Grun, F. Schuth, and K. K. Unger, J. Colloid Interface Sci. **207**, 159 (1998).
[57] A. Vishnyakov, P. I. Ravikovitch, and A. V. Neimark, Langmuir **15**, 8736 (1999).
[58] J. Fischer, U. Heinbuch, and M. Wendland, Mol. Phys. **61**, 953 (1987).
[59] E. Velasco and P. Tarazona, J. Chem. Phys. **91**, 7916 (1989).
[60] A. Z. Panagiotopoulos, Mol. Phys. **61**, 813 (1987).
[61] A. Z. Panagiotopoulos, Mol. Phys. **62**, 701 (1987).
[62] Z. X. Tang, L. E. Scriven, and H. T. Davis, J. Chem. Phys. **95**, 2659 (1991).
[63] L. Mederos, G. Navascues, P. Tarazona, and E. Chacon, Phys. Rev. E **47**, 4284 (1993).
[64] E. Bruno, C. Caccamo, and P. Tarazona, Phys. Rev. A **35**, 1210 (1987).
[65] B. Widom, J. Chem. Phys. **39**, 2808 (1963).
[66] R. Evans, Adv. Phys. **28**, 143 (1979).
[67] J. D. Weeks, D. Chandler, and H. C. Andersen, J. Chem. Phys. **54**, 5237 (1971).
[68] J. A. Barker and D. Henderson, J. Chem. Phys. **47**, 4714 (1967).
[69] J.-P. Hansen and I. R. McDonald, *Theory of Simple Liquids* (Academic, London, 1986).
[70] R. D. Groot and J. P. Vandereerden, Phys. Rev. A **36**, 4356 (1987).
[71] M. Calleja and G. Rickayzen, Mol. Phys. **79**, 809 (1993).
[72] Y. Rosenfeld, Mol. Phys. **94**, 929 (1998).
[73] Y. Rosenfeld, M. Schmidt, H. Lowen, and P. Tarazona, Phys. Rev. E **55**, 4245 (1997).
[74] S. Phan, E. Kierlik, M. L. Rosinberg, B. Bildstein, and G. Kahl, Phys. Rev. E **48**, 618 (1993).
[75] N. F. Carnahan and K. E. Starling, J. Chem. Phys. **51**, 635 (1969).
[76] A. V. Neimark, Langmuir **11**, 4183 (1995).
[77] J. K. Percus and G. J. Yevick, Phys. Rev. **110**, 1 (1958).
[78] P. Tarazona, Phys. Rev. Lett. **84**, 694 (2000).
[79] J. K. Percus, J. Stat. Phys. **15**, 505 (1976).
[80] A. Gonzalez, J. A. White, and R. Evans, J. Phys.: Condens. Matter **9**, 2375 (1997).
[81] L. Verlet and J. J. Weis, Phys. Rev. A **5**, 939 (1972).
[82] B. Q. Lu, R. Evans, and M. M. T. Da Gama, Mol. Phys. **55**, 1319 (1985).
[83] M. P. Allen and D. J. Tildesley, *Computer Simulation of Liquids* (Clarendon, Oxford, 1987).
[84] J. K. Johnson, J. A. Zollweg, and K. E. Gubbins, Mol. Phys. **78**, 591 (1993).
[85] B. K. Peterson and K. E. Gubbins, Mol. Phys. **62**, 215 (1987).
[86] V. Y. Gusev, in *Microscopic Simulation of Interfacial Phenomena in Solids and Liquids* (Ref. [46]), p. 35.

[87] A. V. Neimark and A. Vishnyakov, Phys. Rev. E **62**, 4611 (2000).
[88] W. A. Steele, *The Interactions of Gases with Solid Surfaces* (Pergamon, New York, 1974).
[89] G. J. Tjatjopoulos, D. L. Feke, and J. A. Mann, J. Phys. Chem. **92**, 4006 (1988).
[90] S. Angus, *International Thermodynamic Tables of the Fluid State—6, Nitrogen* (Pergamon, Oxford, 1997).
[91] V. A. Rabinovich, A. A. Vasserman, V. I. Nedostup, and L. S. Veksler, *Thermophysical Properties of Neon, Argon, Krypton, and Xenon* (Hemisphere, Washington, DC, 1988).
[92] C. L. Yaws, *Physical Properties* (McGraw-Hill, New York, 1997).
[93] M. Mecke, J. Winkelmann, and J. Fischer, J. Chem. Phys. **107**, 9264 (1997).
[94] F. Rouquerol, J. Rouquerol, and K. S. W. Sing, *Adsorption by Powders and Porous Solids* (Academic, San Diego, 1999).
[95] M. W. Maddox, J. P. Olivier, and K. E. Gubbins, Langmuir **13**, 1737 (1997).
[96] J. H. Deboer, B. G. Linsen, and T. J. Osinga, J. Catal. **4**, 643 (1965).
[97] MC data for such wide pores are not available.
[98] P. I. Ravikovitch and A. V. Neimark, Stud. Surf. Sci. Catal. **129**, 597 (2000).
[99] A. Gonzalez, J. A. White, F. L. Roman, and R. Evans, J. Chem. Phys. **109**, 3637 (1998).
[100] D. H. Everett, in *The Solid-Gas Interface*, edited by E. A. Flood (Marcel Dekker, New York, 1967), Vol. 2.
[101] A. V. Neimark and P. I. Ravikovitch, Stud. Surf. Sci. Catal. **128**, 51 (2000).
[102] A. V. Neimark and P. I. Ravikovitch, Micropor. Mesopor. Mater. **44–45**, 697 (2001).
[103] P. I. Ravikovitch and A. V. Neimark, Coll. Surf., A (to be published).
[104] M. Kruk, M. Jaroniec, and A. Sayari, Langmuir **13**, 6267 (1997).
[105] A. Vishnyakov, E. M. Piotrovskaya, and E. N. Brodskaya, Adsorption **4**, 207 (1998).
[106] M. W. Maddox and K. E. Gubbins, J. Chem. Phys. **107**, 9659 (1997).
[107] M. Miyahara and K. E. Gubbins, J. Chem. Phys. **106**, 2865 (1997).
[108] H. Dominguez, M. P. Allen, and R. Evans, Mol. Phys. **96**, 209 (1999).
[109] R. Radhakrishnan and K. E. Gubbins, Mol. Phys. **96**, 1249 (1999).
[110] P. I. Ravikovitch (unpublished).
[111] M. J. Bojan and W. A. Steele, Carbon **36**, 1417 (1998).
[112] S. J. Gregg and K. S. W. Sing, *Adsorption, Surface Area and Porosity* (Academic, New York, 1982).